

THESIS

CONNECTIONS BETWEEN CLIMATE SENSITIVITY AND LARGE-SCALE
EXTRATROPICAL DYNAMICS

Submitted by

Luke L. B. Davis

Department of Atmospheric Science

In partial fulfillment of the requirements

For the Degree of Master of Science

Colorado State University

Fort Collins, Colorado

Spring 2019

Master's Committee:

Advisor: David W. J. Thompson

Co-Advisor: Thomas Birner

David A. Randall

Olivier Pinaud

Copyright by Luke L. B. Davis 2019

All Rights Reserved

ABSTRACT

CONNECTIONS BETWEEN CLIMATE SENSITIVITY AND LARGE-SCALE EXTRATROPICAL DYNAMICS

The response of the extratropical storm tracks to anthropogenic forcing is one of the most important but poorly understood aspects of climate change. The direct, thermodynamic effects of climate change are relatively well understood, but their two-way interactions with large-scale extratropical dynamics are extremely difficult to predict. There is thus continued need for a robust understanding of how this coupling evolves in space and time.

The dry dynamical core represents one of the simplest possible numerical models for studying the response of the extratropical storm tracks to climate change. In the model, the extratropical circulation is forced by relaxing to a radiative equilibrium profile using linear damping. The linear damping coefficient plays an essential role in governing the structure of the circulation. But despite decades of research with the dry dynamical core, the role of the damping coefficient in governing the circulation has received relatively little scrutiny.

In this thesis, we systematically vary the damping rate and the equilibrium temperature field in a dry dynamical core in order to understand how the amplitude of the damping influences extratropical dynamics. Critically, we prove that the damping rate is a measure of the climate sensitivity of the dry atmosphere. The key finding is that the structure of the extratropical circulation is a function of the climate sensitivity. Larger damping timescales – which are equivalent to higher climate sensitivities – lead to a less dynamically active extratropical circulation, equatorward shifts in the jet, and a background state that is almost neutral to baroclinic instability. They also lead to increases in the serial correlation and relative strength of the annular modes of climate variability. It is argued that the climate sensitivity of the dry atmosphere may be identifiable from its dynamical signatures, and that

understanding the response of the circulation to climate change is critically dependent on understanding its climate sensitivity.

ACKNOWLEDGEMENTS

This thesis was supported by the U.S. National Science Foundation Climate Dynamics Program, award number 1643167.

I would like to thank my advisors, David W. J. Thompson and Thomas Birner, for their guidance, their kindness, and their patience over the past two years. I would like to thank professors David A. Randall, Isaac Held, Christine Chiu, and Elizabeth Barnes for their contributions and insight. I would like to thank my student colleagues in the Department of Atmospheric Science for fostering a healthy, collaborative work atmosphere, and for their friendship in stressful times.

I would like to thank my maternal grandparents, Vivianne T. Nachmias and Jacob Nachmias, former professors at the University of Pennsylvania, for inspiring me to pursue a career in science from a young age, and for their financial support through years of education. In this regard I'm also indebted to my paternal grandparents, I. Ridgway Davis and Margaret M. Davis, may they rest in peace. Finally I'd like to thank my mother, Lisa N. Davis, for her support, her courage, and for the sacrifices she made to get me where I am today.

TABLE OF CONTENTS

ABSTRACT	ii
ACKNOWLEDGEMENTS	iv
LIST OF TABLES	vi
LIST OF FIGURES	vii
Chapter 1 Introduction	1
1.1 Variability, change, and the extratropics	1
1.2 Insight from simple models	3
1.3 This work	5
Chapter 2 On thermal damping	6
2.1 Damping and real-world processes	6
2.2 The equivalency of damping and climate sensitivity	9
2.2.1 Review	9
2.2.2 Proof	10
2.2.3 Implications	12
Chapter 3 Methods	15
3.1 The dry dynamical core	15
3.2 Model parameterizations	16
3.3 Experiments	18
Chapter 4 Results	23
4.1 Overview	23
4.2 Wave driving and propagation	33
4.3 Subtropical and eddy-driven jets	40
4.4 Climate variability and eddy-mean feedbacks	44
Chapter 5 Discussion	49
5.1 Review	49
5.2 Conclusions	50
5.3 Future work	51
Bibliography	53
Appendix A Background	61
A.1 Lorenz energy budgets	61
A.2 Spectral decompositions	63
A.3 Annular modes	64

LIST OF TABLES

3.1	Overview of the parameters controlling thermal damping in the dry dynamical core. See text for details.	17
3.2	Description and naming conventions for the various experiment series. See text for further details.	22
A.1	Notation for the Lorenz energy cycle definitions.	62

LIST OF FIGURES

2.1	(shading) 1981-2010 averages of diabatic heating rates estimated by the ERA-Interim reanalysis forecasts in January (top-left) and July (top-right), and the 5000-day average diabatic heating rates simulated by the equinoctial HS94 configuration of the dry dynamical core (bottom). Black contours indicate potential temperature, and the gray contours indicate the American Meteorological Society definition of the tropopause (i.e. the 2K/km lapse rate height).	7
2.2	Climate sensitivity to a $2\times\text{CO}_2$ -equivalent heating (estimated as 3.7 W m^{-2}) for the dry atmosphere. The star and dashed black lines highlight the climate sensitivity given a 40 day damping timescale. See text for details.	13
3.1	(left, shading) The equilibrium temperature, (left, contours) equilibrium potential temperature, and (right) thermal damping timescales for the HS94 configuration of the dry dynamical core. See text for details.	18
3.2	(left, black) Eady growth rate averaged between latitudes $20\text{-}70^\circ$, pressures 1000-500hPa; (right, red) eddy heat flux averaged over the same region. Solid lines (thick dashed lines) correspond to experiments where the full damping rate (zonal-mean damping rate) was changed. Gray shading indicates where the thermal damping rate (i.e. the inverse thermal damping timescale) is greater than the Eady growth rate. The plus sign indicates where the KATMOS2 experiment series crosses this threshold.	21
4.1	(shading) Zonal-mean diabatic heating rates and (contours, units K) potential temperature for the ATOMS-MEAN parameter sweep. Note that the heating rate scale is non-linear. The gray contour indicates the AMS tropopause (i.e. the lowest level with 2K/km vertical lapse rate). Each panel represents the average of the southern and northern hemisphere 5000-day climatologies. The thermal damping timescales are increasing from top-left to bottom-right in column-major order, and are indicated in the top-left corner of each plot. The panel outlined in red indicates the HS94 value of 40 days.	24

4.2	Parametric depictions of diabatic heating across the parameter sweep experiments. The colors red, blue, and gray correspond to the KATMOS, KATMOS-MEAN, and TGRAD experiments, respectively. Each colored “block” corresponds to an individual 5000-day climatology. As indicated by the legend, dashed red/blue lines correspond to the KATMOS1 and KATMOS1-MEAN experiments (in which damping is constant throughout the atmosphere), and solid red/blue lines correspond to the KATMOS2 and KATMOS2-MEAN experiments (in which the boundary layer damping is stronger); see Table 3.2 for details. The following metrics are plotted relative to the bulk horizontal temperature difference $\Delta\Theta_h$ (see text): (left) the ratio of the equilibrium equator-pole temperature difference $\Delta\Theta_{h,eq}$ to $\Delta\Theta_h$; (middle) the average extratropical cooling rate over 50° - 90° latitude and 850-250hPa; and (right) the average boundary layer heating rate over 10° - 40° latitude and 1000-850hPa.	25
4.3	As in Figure 4.1, but for the eddy heat flux (shading) and isentropic slope (contours, units m/km). This time, the color scales in each panel are normalized by the values indicated at the bottom-left.	27
4.4	As in Figure 4.2, but comparing $\Delta\Theta_h$ against (top-left) the bulk surface-tropopause potential temperature difference $\Delta\Theta_v$; (top-right) the ratio $\Delta\Theta_h/\Delta\Theta_v$; and (bottom) the maximum eddy heat flux averaged between 1000hPa and 500hPa. Dashes black lines indicate (top-left) constant criticality and (bottom) constant diffusivity.	28
4.5	As in Figure 4.1, but showing eddy potential vorticity fluxes (shading) and zonal-mean potential vorticity (contours, units PVU) in <i>isentropic</i> coordinates. This time the solid gray contour indicates the 2PVU “dynamical” tropopause. The thin, dashed contours indicate the 5th, 20th, 50th, 80th, and 95th percentile surface potential temperatures.	29
4.6	Lorenz energy budget terms for the different sweep experiments, as a function of the bulk meridional temperature gradient $\Delta\Theta_h$. Boxes in red indicate energy content terms (units MJ m^{-2}), and boxes in gray indicate energy transfer terms (units W m^{-2}). From left-to-right, the top row shows (1) the mean (diabatic) generation of available potential energy (APE); (2) the mean APE; (3) the conversion from mean kinetic energy to mean APE; (4) the mean kinetic energy; and (5) the frictional dissipation of mean kinetic energy. The third row is as in the first row, but for the eddy components, and with the conversion term positive in the direction of potential-kinetic energy conversion. The second row shows conversion from (left) mean APE to eddy APE, and (right) eddy kinetic energy to mean kinetic energy. The bottom row shows the sum of the eddy and mean components of APE generation, APE, APE-kinetic energy conversion, kinetic energy, and dissipation of kinetic energy. The notation in the top-right corner of each panel matches Oort (1964) [53].	31
4.7	As in Figure 4.6, but with the extratropical diabatic cooling rates on the x -axis. The cooling rates were averaged over 50° - 90° latitude, 400-800hPa.	32
4.8	As in Figure 4.1, but for the EP flux divergence (shading) and components of the EP flux vectors (arrows). The scaling is as in Andrews (1987) [2].	34

4.9	As in Figure 4.2, but showing averages over 10° - 40° latitude of the pressure levels for the (left) thermodynamic tropopause (i.e. the 2K/km lapse rate) and (right) the mass transport-defined tropopause (i.e. the height at which the residual mass streamfunction reaches 10% of its maximum value).	35
4.10	As in Figure 4.2, but with the x -axis indicating the power-weighted, mass-weighted average zonal wavelength (units km) from the spectral decomposition of the meridional wind anomalies between 500hPa and 1000hPa. The y -axis on the top-left panel indicates the bulk static stability $\Delta\Theta_v$, and the remaining 3 panels show predictive length-scale metrics: the (top-right) Rhines β -scale L_R , (bottom-left) Rossby deformation radius L_d , and the “displacement” length scale L_{disp}	37
4.11	As in Figure 4.3, but instead showing the (shading) co-spectral power of the 500hPa Eliassen-Palm (EP) flux divergence and (contours, units m^2/s^2) spectral power of the 500hPa meridional wind anomalies as a function of phase speed (x -axis) and latitude (y -axis). The red contour indicates the 500hPa zonal-mean zonal wind.	39
4.12	As in Figure 4.3, but for the (shading) eddy momentum flux convergence and (contours, units m/s) zonal-mean zonal wind in the KATMOS2-MEAN experiment.	41
4.13	Jet stream analysis for the (top) KATMOS1-MEAN and (bottom) TGRAD experiments. Red lines correspond to the eddy-driven jet, detected from (solid red) local maxima in eddy-momentum flux convergence forcing and (pale red) surface wind maxima. Blue lines correspond to the subtropical jet, detected from (solid blue) local maxima in vertically-averaged thermal wind and (pale blue) maxima in vertically averaged shear. Left panels show <i>latitudes</i> of the maxima across the experiment climatologies. Right panels show the normalized <i>strengths</i> of these maxima. The x -axes correspond to the forcing parameter ($\bar{\tau}_t$ for KATMOS1-MEAN, $\Delta\Theta_{h,\text{eq}}$ for TGRAD). For a single experiment (i.e. a single point on the x -axis), multiple lines indicate the presence of multiple jets.	42
4.14	As in Figure 4.2, but comparing the latitude of the eddy-driven jet (defined as the latitude of maximum integrated eddy-momentum flux convergence) to the strength of the maximum eddy-momentum flux convergence.	43
4.15	As in Figure 4.3, but showing the (shading) first and (contours) second EOFs of eddy kinetic energy.	46
4.16	As in Figure 4.2, but showing the percent variance explained by the annular modes as a function of the bulk meridional temperature gradient $\Delta\Theta_h$. The top row shows the variance explained by the SAM and BAM in their respective fields (mean kinetic energy and eddy kinetic energy), and the bottom row shows the variance in eddy momentum flux convergence and isentropic slope explained by the <i>forcing patterns</i> associated with the annular modes in the top row. See section A.3 for details.	47

4.17 Autocorrelation timescales for the annular modes in the (left) KATMOS1 and KATMOS1-MEAN experiments, and (right) KATMOS2 and KATMOS2-MEAN experiments, as a function of the damping timescale τ_t . The black lines (left y -axes) indicate the SAM timescales, and the red lines (right y -axes) indicate the BAM timescales. 48

Chapter 1

Introduction

1.1 Variability, change, and the extratropics

Anthropogenic climate change is expected to have wide-ranging effects on the general circulation. Over the past decade, the climate science community has tried to predict these effects using a combination of theoretical arguments and general circulation models of the atmosphere (GCMs). Many of these effects are fairly robust – for example, the tropical belt is expected to widen with climate change (Kirtman et al., 2013 [42]; Lu et al., 2007 [46]); the hydrological cycle is expected to accelerate (the so-called “wet get wetter, dry get drier” hypothesis; Held and Soden, 2006 [36]); and the extratropical tropopause is expected to rise (Santer et al., 2003 [58]). These changes can be related quite directly to three simple facts: the amount of carbon dioxide in the atmosphere will increase, the atmosphere will warm, and the amount of water vapor in the atmosphere will increase.

Extratropical dynamics, however, are more complicated. In the extratropics, the atmosphere is baroclinic: waves intensify according to highly non-linear life cycle processes (e.g. Simmons and Hoskins, 1978 [64]), generating the large majority of equator-to-pole heat transport and sustaining a thermodynamically indirect overturning circulation. Eddies are generated near the surface, propagating upward and outward, and finally dissipated in the extratropical and subtropical upper troposphere (Andrews and McIntyre, 1976 [4], Schneider, 2006 [60]). Consequent eddy fluxes of momentum drive the so-called eddy-driven jet – a band of westerly near-surface winds beneath the storm track region. The strength and position of eddy fluxes of heat and momentum vary over timescales much longer than the eddy growth timescales. The larger part of this variability can be described by so-called annular or “dynamical” modes (Hartmann and Lo, 1998 [32], Thompson and Wallace, 2000

[69]), whose persistence is owed to eddy feedbacks on the mean background state (Lorenz and Hartmann, 2001 [44], Feldstein and Lee, 1998 [22]).

The intensity and distribution of the extratropical storms has been described from a wide variety of physical perspectives. Perhaps the simplest is the *Lorenz cycle*, which views the extratropical eddies as tapping into (and limited by) a global reservoir of potential energy, thereupon converting it to kinetic energy and dissipating it via friction (Lorenz, 1955 [45], Oort, 1964 [53]). Another common perspective holds that eddy production and dissipation are constrained by the suitability of the background environment for wave propagation, with the storm track region bounded by “critical” and “turning” latitudes (the “extratropical waveguide”; e.g. Randel and Held, 1991 [55], Chen Gang and Held Isaac M., 2007 [17]). The macroturbulence perspective holds that baroclinic eddies can be viewed as a manifestation of turbulence, characterized by a limited upscale energy cascade (Held, 1999 [34]). The finite-amplitude wave perspective extends the thinking behind “diffusive closures” to flows with macroscopic waves and *non-linear* eddy-mean flow interactions (Andrews, 1983 [1], Nakamura and Zhu, 2010 [52]) The “true” physical description of the extratropical circulation lies in some combination of these perspectives.

In summary, the extratropics are characterized by a combination of highly non-linear eddy growth processes with slowly evolving modes of variability. All of these processes are sensitive to subtle adjustments in static stability and horizontal temperature gradients. This paints a fuzzy picture of expected changes to the strength, and even perhaps the position, of the storm track region in response to global warming (Shaw et al., 2016 [61]). These processes are also coupled to changes outside of the troposphere, like small-scale ocean fronts (Small et al., 2008 [65]; Nakamura et al., 2013 [51]), larger-scale changes to sea-surface temperature gradients (Brayshaw et al., 2008 [13]), and stratospheric winds and static stability (Shepherd, 2002 [62]).

Unfortunately, there is so far no comprehensive theory for the relationship between the extratropical eddies and their background state. We know that the mean flow response to

thermal forcing is expressed strongly in the dominant modes of internal variability (Ring and Plumb, 2007 [56]; Thompson et al., 2000 [70]). We also know that the latitude and intensity of eddy fluxes can be estimated from the projection of the forcing onto the background baroclinicity, under a diffusive assumption (Butler et al., 2010 [15]; Butler et al., 2011 [14]). But there is no guarantee how the ensemble of spatially and temporally varying changes to temperature, diabatic heating, thermal stratification, and meridional temperature gradients will modify the storm track position and intensity (Shaw et al., 2016 [61]). A complicating factor is the weak diabatic coupling between barotropic and baroclinic processes (Boljka and Shepherd, 2018 [11]; Boljka et al., 2018 [12]).

Even if we can predict the changes to static stability and baroclinicity owing to strictly thermodynamic processes, it is not guaranteed how the eddies will modify and interact with these changes. There is a continued need for experimentation with simple models to understand how the extratropical circulation may respond to climate change.

1.2 Insight from simple models

For much of the late 20th century, much of the climate science community was largely focused on increasing model sophistication and model resolution – in essence, more parameterizations and more grid cells. Unfortunately, this sophistication comes at the expense of tractability. Broadly speaking, the more complex the model, the more confounding factors – and therefore, the harder it is to gain theoretical insight from said model.

Increasingly so, there was a need for models with intentionally limited complexity, so that phenomena observed in the “model world” could be understood from the simplest possible set of governing equations. A useful construct in this line of thinking is the “model hierarchy”: a “continuum” of numerical models with monotonically increasing complexity, from which the simplest possible model for a given research question can be selected. Jeevanjee et al. (2017) [40] provide an excellent review of the model hierarchy for the general circulation of the atmosphere, and an open-source standard for this hierarchy was released by Vallis et al.

(2018) [71]. The so-called “dry dynamical core” – the part of the model that integrates the primitive equations of motion on the rotating sphere – lies near the base of this hierarchy. Since the dry core simulates only conservative dynamics, it must be coupled with a suite of parameterizations for non-conservative processes, the most popular of which was formalized by Held and Suarez (1994) [37] (hereafter HS94).

The revival of the simple model (and the dry dynamical core in particular) began a wave of research that has greatly improved our understanding of extratropical dynamics. Haynes et al. (2001) [33] used the dry core to study the so-called “self-organization” of the extratropical flow by the stirring effects of eddies (the spontaneous formation of a sharp extratropical tropopause). Schneider (2004) [59] used the dry core to test a proposed dynamical constraint on the extratropical tropopause height: the equivalency of the extratropical surface-tropopause potential temperature difference and the equator-pole surface temperature difference. Polvani and Kushner (2002) [54] investigated the relationship between the jet stream position and the polar vortex strength. Butler et al. (2010) [15] and Butler et al. (2011) [14] investigated the response of eddy fluxes and the isentropic slope to climate change-like thermal forcings, and Mbengue and Schneider (2013) [49] explored how changes to static stability and surface temperature affect the storm track in the absence of moisture. Baker et al. (2017) [7] used the dry core to test the circulation response to the systematic application of spatially localized heating perturbations throughout the troposphere. Chen et al. (2007) [16] used the dry core to study the relationship between surface friction and the jet stream position and strength. “Parameter sweeps” are a common starting point for these types of analyses, in which the strength of some imposed perturbation or intrinsic parameterization is systematically varied to understand its effect on the circulation.

As one of the simplest possible representations of atmospheric dynamics, the dry core has been rigorously tested over the past few decades. In particular, the parameterizations used to stand in for non-conservative processes have been modified in a variety of studies (either as the means for answering another scientific question, or as the point of interest itself). However

in our opinion, despite its significance to the thermodynamics of the dry atmosphere, the thermal damping parameterization – and, in particular, the thermal damping timescale (see section 3.2) – has received relatively little attention. This constitutes our motivation: To understand what can be learned about extratropical dynamics from simple thermal damping in the dry dynamical core.

1.3 This work

In this thesis, we detail the physical connections between idealized thermal damping and the real world. In particular, we demonstrate that the thermal damping timescale plays the role of the *climate sensitivity* of the dry atmosphere. We then replicate the results of Zurita-Gotor (2008) [72] (hereafter Z08) with a systematic review of the changes to the extratropical circulation associated with changes to the thermal damping parameterization. We add to this an analysis of the changes to *climate variability* and storm track intensity associated with the thermal damping timescale. We conclude with a discussion of how the extratropical response to climate sensitivity in the dry core can be differentiated from the response to changing "equilibrium temperature" (analogous to changing the radiative equilibrium, i.e. a "global warming" scenario).

In chapter 2, we quantify the relationship between thermal damping and the *climate sensitivity* of the dry atmosphere, and discuss its implications. In chapter 3, we describe the model setup, the HS94 configuration, and the experiments used to test the impact of thermal damping (i.e., climate sensitivity) on the extratropical circulation. We describe our results in detail in chapter 4, and in chapter 5, we outline the key results and consider plans for future work.

Chapter 2

On thermal damping

2.1 Damping and real-world processes

Thermal damping in the dry dynamical core, described in detail in section 3.2, is not meant to stand in for any particular process. It was chosen as the *simplest possible* formulation that successfully reproduces the observed diabatic heating climatology; in the real world, this heating is driven by a suite of complex processes. Nevertheless, the rich set of results described in chapter 4 encourages us to consider how thermal damping may relate to these processes.

Figure 2.1 shows the mean diabatic heating rates estimated by the ERA-Interim reanalysis (Dee et al., 2011 [20]) in January (top-left) and July (top-right), along with diabatic heating rates from the HS94 configuration of the dry dynamical core (bottom). The reanalysis “heating rates” are the 1981-2010 averages of 12-hour accumulated temperature changes due to physics parameterizations predicted by the ERA-Interim forecast model, divided by 12 hours. We see that the intensity of observed diabatic heating over the rising branch of the Hadley cell (i.e. the ITCZ) is much greater than the diabatic heating observed in the dry core, owing to moist convection. We also notice that average heating rates in the dry core are always negative outside of ± 20 degrees latitude and above 800hPa, while the observations indicate bands of net positive heating around the storm track region of the extratropics, owing to latent and sensible heat fluxes. In spite of these differences, the winter-time observations are *broadly* in agreement with the dry core simulation: there is (1) net diabatic heating in the boundary layer, generally growing stronger toward the equator; (2) net diabatic heating in the rising branch of the Hadley cell; and (3) *on average*, net diabatic cooling over the subtropical and extratropical free atmosphere.

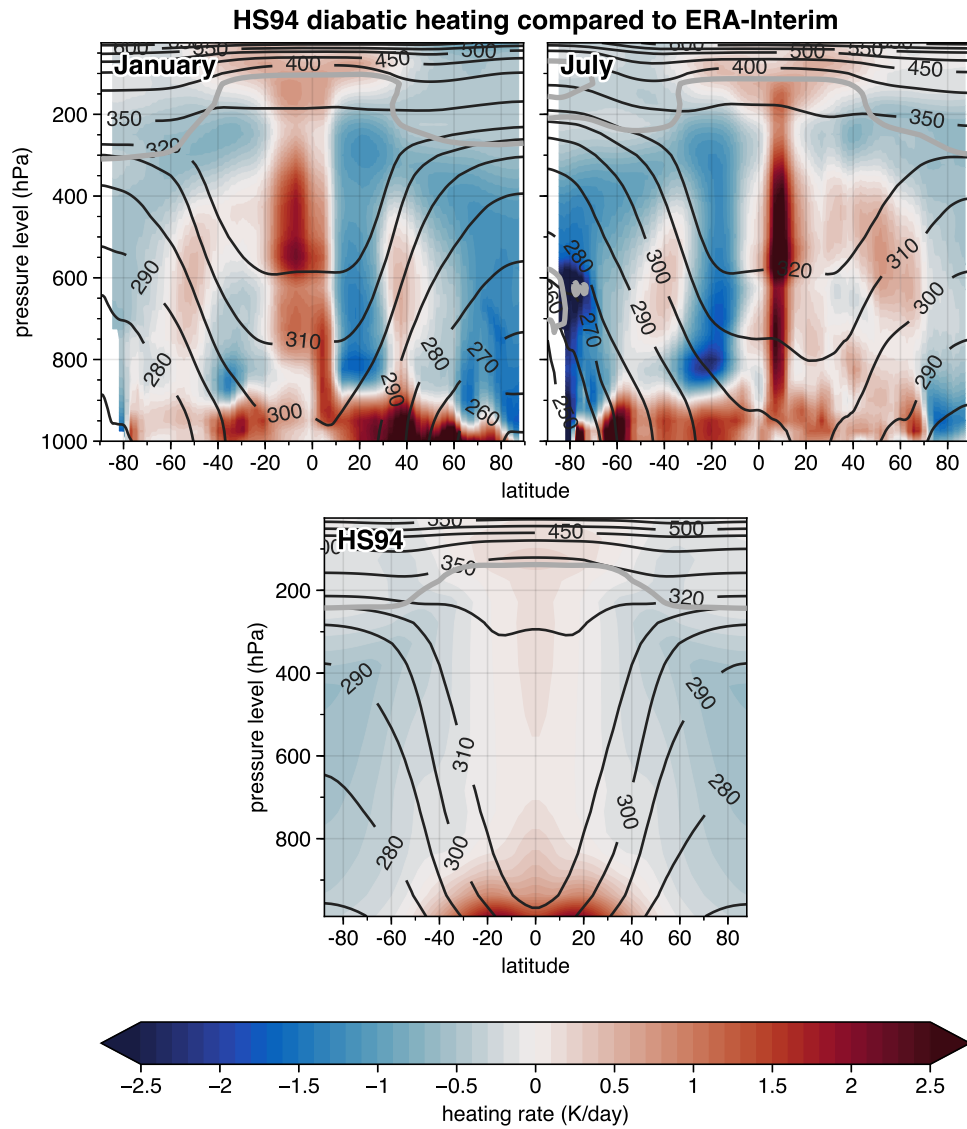


Figure 2.1: (shading) 1981-2010 averages of diabatic heating rates estimated by the ERA-Interim reanalysis forecasts in January (top-left) and July (top-right), and the 5000-day average diabatic heating rates simulated by the equinoctial HS94 configuration of the dry dynamical core (bottom). Black contours indicate potential temperature, and the gray contours indicate the American Meteorological Society definition of the tropopause (i.e. the 2K/km lapse rate height).

In light of these similarities, it is worth noting that some of our results are reminiscent of GCM experiments with more “realistic” diabatic parameterizations. Lucarini et al. (2010) [47] describe a linear relationship between the logarithm of CO₂ concentration and the intensity of the Lorenz energy cycle, due to the intensification of tropospheric radiative cooling – similar to our results with increased damping (cf. Figure 4.6). Likewise, Juckes (2000) [41] and Frierson (2008) [25] describe an increase in static stability (and corresponding reduction in isentropic slope) associated with the moistening of the atmosphere, which enhances latent heat transfer and reduces tropospheric diabatic cooling overall – similar to our results with reduced damping (see Figure 4.4).

We must admit that as a conceptual model for cooling in the troposphere, linear relaxation is inadequate. Since the “radiative equilibrium” temperature profile is statically unstable (Manabe and Strickler (1964) [48]), linear relaxation to such a state would of course be interrupted by convective instability – we compensate for this by using a statically stable “equilibrium temperature”. Further, because the troposphere is optically thick, radiative exchange between adjacent atmospheric layers cannot be neglected (Modest (2013) [50]) – which means the “cooling-to-space” approximation (resembling linear relaxation) is insufficient. However linear relaxation may be adequate in the oceanic boundary layer, where the temperature tendency can resemble a relaxation to ocean surface temperature owing to their differences in heat capacity (e.g. Frankignoul (1985) [23], Frankignoul et al. (1998) [24]). And in the stratosphere, since mean stratospheric temperatures are generally close to radiative equilibrium and the optical thickness is very low, upwards of 80% of the total variance in diabatic heating can be explained by a linear relaxation term (Andrews et al. (1987) [3], Hitchcock et al. (2009) [38]).

In summary, we have identified similarities between (1) the dry core and ERA-Interim diabatic heating climatologies; and (2) the thermal damping parameterization and certain real-world physical processes. Given these similarities, we can imagine devising experiments resembling those discussed in chapter 3 for more complex GCMs. For example, by changing

the efficiency of atmosphere-ocean heat exchange, or by changing the abundance of CO₂ and H₂O in the troposphere and stratosphere, we might expect an extratropical response similar to the response to changing the thermal damping rate. We see that “thermal damping” may be a reasonable starting point for investigating how the circulation will respond to a changing landscape of diabatic processes.

2.2 The equivalency of damping and climate sensitivity

A particularly appealing characteristic of “thermal damping” is its simple relationship with *climate sensitivity*. But before we dive into the proof, a brief review is in order.

2.2.1 Review

Taken together, the ocean, atmosphere, and surface can be described as a thermodynamic system in disequilibrium. The internal energy of this system, which we term the *climate system*, is continually changing via two mechanisms: The addition of heat resulting from solar radiation absorption, and loss of heat resulting from thermal radiation emission. Therefore, the rate of change of the internal energy of the climate system must be equivalent to the difference between incoming radiation and outgoing radiation at the top of the dynamically active part of the atmosphere (i.e., the *troposphere*). The global average of this difference is the so-called *radiative forcing*.

If we impose a positive radiative forcing, in the absence of atmospheric motions, the Earth system will warm until outgoing thermal radiation balances the forcing – the so-called *Planck feedback*. However, the Earth system is complex, and the Planck feedback activates a variety of other feedbacks that individually act to amplify or reduce the radiative imbalance. The average temperature change at the Earth’s surface as a result of all of these interacting feedbacks is called the *equilibrium climate sensitivity*.

In the real world, the equilibrium climate sensitivity is set by an array of physical processes, the most relevant being the water vapor feedback, the oceanic heat uptake feedback,

the tropical lapse rate feedback, the ice-albedo feedback, and the cloud-albedo, cloud-height, and cloud-coverage feedbacks (e.g. Hansen et al., 1984 [30]). As such, the equilibrium climate sensitivity cannot be determined analytically; we must use general circulation models and simplified theoretical arguments to estimate the sensitivity. However for the uncoupled dry atmosphere, it turns out the climate sensitivity is set entirely by a single, fixed parameter: the *thermal damping timescale*.

2.2.2 Proof

Our discussion of climate sensitivity thus far begs the question: what is the equilibrium climate sensitivity for a world with no “radiative forcing” (i.e. no parameterized radiation) and no “surface” (i.e. no parameterized surface-atmosphere exchange processes)?

In the real atmosphere, positive radiative forcing is associated with increased absorption of outgoing thermal radiation throughout the troposphere. If we suppose the resultant heating is distributed evenly with height at *steady-state*, we can simulate “radiative forcing” by imposing a constant heating term for each model level. With this revised definition of radiative forcing, we prove the “equilibrium climate sensitivity” is a constant multiple of the average thermal damping timescale.

At steady-state, the global response to radiative forcing is described by the feedback parameter (e.g. Armour et al., 2012 [6]; Roe and Baker, 2007 [57])

$$\lambda \equiv \frac{Q}{[\Delta T_{\text{sfc}}]}$$

where ΔT_{sfc} is the steady-state surface warming or *equilibrium climate sensitivity*, Q is the constant radiative forcing, and λ is the *feedback parameter*. The square brackets denote a global, steady-state average.

In the dry atmosphere, the thermodynamic equation for a given layer with height thickness Δz and pressure thickness Δp can be written

$$\begin{aligned}
H &\equiv c_p \partial_t T = -\Delta z \cdot c_p \rho \left(\frac{T - T_{\text{eq}}}{\tau} \right) + X + Y \\
&= -\Delta p \cdot c_p g^{-1} \left(\frac{T - T_{\text{eq}}}{\tau} \right) + X + Y
\end{aligned} \tag{2.1}$$

where H is the local rate of change of enthalpy, c_p is the specific heat capacity, τ and T_{eq} are the thermal damping timescale and equilibrium temperature field, respectively (see section 3.2 for details), X is the adiabatic heating, and Y is the advective heating. The second line makes the hydrostatic approximation.

If we take the global, steady-state mean of Equation 2.1, the adiabatic and advective heating terms vanish. In the absence of forcing, the thermodynamic equation becomes

$$\begin{aligned}
[H]_i &\equiv 0 = -\Delta p_i \cdot c_p g^{-1} \left[\tau^{-1} (T - T_{\text{eq}}) \right]_i \\
\left[\tau^{-1} T \right]_i &= \left[\tau^{-1} T_{\text{eq}} \right]_i
\end{aligned} \tag{2.2}$$

i.e. the damping-weighted, steady-state global mean temperature at each height equals the damping-weighted global mean *equilibrium* temperature. Note that if τ^{-1} is constant for level i , this reduces to $[T]_i \equiv [T_{\text{eq}}]_i$. Also note this implies weaker damping supports larger steady-state disequilibria, as expected.

Next, we impose the layer-wise forcing Q_i . Again in the global, steady-state mean, the thermodynamic equation becomes

$$\begin{aligned}
[H]_i &\equiv 0 = Q_i - \Delta p_i \cdot c_p g^{-1} \left(\left[\tau^{-1} T \right]_{i,\text{forced}} - \left[\tau^{-1} T_{\text{eq}} \right]_i \right) \\
&= Q_i - \Delta p_i \cdot c_p g^{-1} \left(\left[\tau^{-1} T \right]_{i,\text{forced}} - \left[\tau^{-1} T \right]_{i,\text{unforced}} \right)
\end{aligned}$$

where the second line uses Equation 2.2. If we define a “damping-weighted” climate sensitivity as follows:

$$\Delta T_{\text{atmos}}^* \equiv \frac{\left[\tau^{-1} T \right]_{i,\text{forced}} - \left[\tau^{-1} T \right]_{i,\text{unforced}}}{\left[\tau^{-1} \right]_i},$$

we find

$$\Delta T_{\text{atmos},i}^* \equiv \frac{gQ_i}{c_p \Delta p_i} [\tau^{-1}]_i^{-1} \quad (2.3)$$

That is, the damping-weighted equilibrium climate sensitivity of model level i is simply a factor of the inverse average damping rate.

If we take the mass-weighted vertical average of Equation 2.3, assuming the layer-wise radiative forcings Q_i are distributed equally as a function of layer mass (i.e. $Q_{\text{top}} \equiv \sum_i Q_i$, where Q_{top} is the net radiative forcing), we find

$$\Delta T_{\text{atmos}}^* \equiv \frac{gQ_{\text{top}}}{c_p p_{\text{sfc}}} \langle [\tau^{-1}] \rangle^{-1}$$

where p_{sfc} is the mean surface temperature and the angle brackets denote a vertical average.

Finally, in the special case of *spatially uniform* damping, the damping-weighted climate sensitivity equals the climate sensitivity exactly; we have

$$\boxed{\Delta T_{\text{atmos}} \equiv \frac{gQ_{\text{top}}\tau}{c_p p_{\text{sfc}}}} \quad (2.4)$$

Equation 2.4 is plotted in Figure 2.2 with a $2\times\text{CO}_2$ -equivalent radiative forcing Q_{top} . With the HS94 default of $\tau = 40$ days, we find a climate sensitivity of around 1.2K. It is striking to note *this is nearly identical to the average “equilibrium” climate sensitivity¹ measured by fully-coupled GCMs* (Roe and Baker, 2007 [57]; Soden and Held, 2006 [66]). Although the HS94 timescale of *40 days* was selected to best reproduce Earth’s steady-state climatology, it appears to also succeed in reproducing Earth’s climate sensitivity.

2.2.3 Implications

In the previous section, we showed that the dry-atmosphere climate sensitivity is a function of the magnitude and spatial structure of the thermal damping timescale. This is not

¹“Equilibrium” climate sensitivity is the global-mean surface temperature response to a radiative forcing in the absence of all feedbacks, except for the Planck feedback.

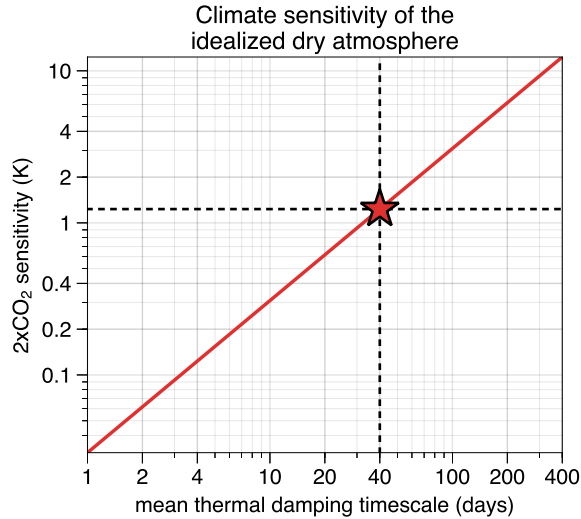


Figure 2.2: Climate sensitivity to a $2\times\text{CO}_2$ -equivalent heating (estimated as 3.7 W m^{-2}) for the dry atmosphere. The star and dashed black lines highlight the climate sensitivity given a 40 day damping timescale. See text for details.

surprising; Armour et al. (2012) [6] demonstrated that “global climate sensitivity” can be cast as the accumulation of spatially and temporally varying local climate feedbacks. The spatial structure of the damping timescale in HS94 is also reminiscent of real-world climate feedback mechanisms – enhanced boundary layer damping resembles the negative ocean heat-uptake feedback (e.g. Hansen et al., 1985 [31]), just as it resembles ocean-atmosphere sensible heat exchange more generally (section 2.1). Similarly, enhanced tropical damping in the Schneider (2004) [59] configuration of the dry core is reminiscent of the negative lapse rate feedback (e.g. Hansen et al., 1984 [30]).

This result also makes sense in the context of fluctuation-dissipation theory (FDT). FDT holds that the response of a dynamical system to an infinitesimal perturbation (i.e. the linearization of the full response) is characterized by the intrinsic modes by which the system dissipates transient perturbations and returns to its steady-state configuration (Leith, 1975 [43]). Bell (1980) [10] show that dissipative terms, when added to a single-layer barotropic model, fulfill this role for *enstrophy*. The thermal restoration term (i.e. the damping rate) may analogously fulfill this role for *temperature* in the 3-dimensional dry atmosphere. FDT

has been used extensively to predict the circulation response to local thermal forcing in complex GCMs (e.g. Gritsun and Branstator, 2007 [28]; Gritsun et al., 2008 [29]; Cionni et al., 2004 [18]). Since the dry dynamical core offers an explicit, *tunable* parameter for the dissipation efficiency, it may be an attractive starting point in our search for a theoretical understanding of the circulation response to climate change.

We make one final note on this subject. We have shown that for the dry atmosphere, the diabatic heating associated with the steady-state circulation is described in the exact same way as the climatological response to radiative forcing. While this may not necessarily be true for the real atmosphere, owing to feedbacks between the dynamical heating terms and the diabatic heating, this does not prohibit us from making the following, generalized statement: *diabatic processes conducive to strong heating rates tend to favor a relatively insensitive climate, and aggregate changes to these processes imply changes to the climate sensitivity.*

Chapter 3

Methods

3.1 The dry dynamical core

The dynamical core solves the prognostic equations for vorticity, divergence, temperature, and surface pressure in spherical harmonic domain². The spherical harmonic transformation simplifies the solutions to the differential equations, analogous to the Fourier transformation of a 1D system of equations. Vertical differentials are solved with the finite differencing method described by Simmons and Burridge (1981) [63].

The prognostic equations can only be solved with a finite number of spherical harmonics. For this study, we retained the first 42 spherical harmonics (i.e. the truncation number is “T42”)³. This gives an equatorial resolution of approximately 2.80° in latitude and longitude, or around 300km. Our results were not found to be sensitive to the truncation number.

Vertical levels in the dry dynamical core are specified in “hybrid” coordinates. For a vertical resolution of N layers (or “full-levels”), hybrid coordinates are defined at the $N + 1$ layer interfaces (or “half-levels”) by

$$p_{k-1/2} = A_{k-1/2} + B_{k-1/2}p_{\text{sfc}}, \quad k = 1, N + 1 \quad (3.1)$$

where p_{sfc} is the surface pressure, $A_{k-1/2}$, $B_{k-1/2}$ are the half-level hybrid coordinates, and A_k , B_k are the full-level coordinates. This reduces to isobaric levels when $B_{k-1/2} \equiv 0$, and “sigma” levels when $A_{k-1/2} \equiv 0$. For this study, we used 20 equally-spaced sigma levels B_k .

²For more information, refer to the `spectral_core.pdf` document at <https://github.com/ExeClim/Isca>.

³For the purpose of computational parallelization, truncation numbers are generally chosen so that the lowest possible number of latitudes that do not alias the harmonics has convenient integer divisors. For example, at T42 truncation, the harmonics are translated to 64 (2^6) latitudes. Note the spacing of the latitudes is defined according to Gaussian quadrature.

Higher vertical resolutions are known to produce annular modes with unrealistically long decorrelation timescales (Gerber and Vallis, 2007 [26]).

3.2 Model parameterizations

As discussed in section 1.2, the dry dynamical core lies near the base of the “hierarchy” for modeling extratropical dynamics. As such, various complex, multi-scale processes must be parameterized as simply as numerically possible. Generally, the dry dynamical core is used with three such parameterizations. See Figure 3.1 and Table 3.1 for a summary of those relevant to the diabatic heating parameterization.

1. Non-conservative mixing (i.e. entropy production via diffusion and turbulence) is replaced with so-called *hyperdiffusion*, or the linear damping of high-order differentials of the vorticity field. This has the effect of smoothing fine-scale filaments of vorticity.
2. Frictional drag is replaced by linearly or quadratically relaxing near-surface winds toward zero. For this study, we used the HS94 linear relaxation:

$$\left(\frac{d\vec{u}}{dt}\right)_m = -\frac{\vec{u}(\lambda, \phi, p, t)}{\tau_m(p)} \quad (3.2)$$

$$\tau_m^{-1}(p) \equiv \begin{cases} 0 & 0 \leq \sigma < \sigma_{\text{top}} \\ \tau_{m,\text{sfc}}^{-1} \left(\frac{\sigma(p, p_{\text{sfc}}) - \sigma_{\text{top}}}{1 - \sigma_{\text{top}}} \right) & \sigma_{\text{top}} \leq \sigma \leq 1 \end{cases} \quad (3.3)$$

where τ_m is the *mechanical damping timescale*, σ_{top} is the top of the “boundary layer” in sigma coordinates, $\tau_{m,\text{sfc}}$ is the maximum frictional damping timescale (realized at the surface), $\sigma \equiv p/p_{\text{sfc}}$ is the vertical sigma coordinate, and p_{sfc} is the surface pressure.

3. Diabatic processes (i.e. radiation, latent and sensible heat fluxes, and interactions of clouds with these processes) are replaced by linearly relaxing the temperature toward a notional “equilibrium” temperature. This parameterization, which we term *thermal*

Table 3.1: Overview of the parameters controlling thermal damping in the dry dynamical core. See text for details.

Name	HS94 value	Description
τ_t	varies	The thermal damping timescale, a function of $\tau_{t,\text{atmos}}$, σ_{top} , and $\tau_{t,\text{sfc}}$.
σ_{top}	0.7	The upper-bound of the “boundary layer” in vertical sigma coordinates.
$\tau_{t,\text{atmos}}$	40 days	The free-atmosphere damping timescale.
$\tau_{t,\text{sfc}}$	4 days	The minimum thermal damping timescale, realized at the surface on the equator.

damping, is the focus of this study. We use the HS94 formulation:

$$\left(\frac{dT}{dt}\right)_t = -\frac{T(\lambda, \phi, p, t) - T_{\text{eq}}(\phi, p)}{\tau_t(\phi, p)} \quad (3.4)$$

$$\tau_t^{-1}(\phi, p) \equiv \begin{cases} \tau_{t,\text{atmos}}^{-1} & 0 \leq \sigma < \sigma_{\text{top}} \\ \tau_{t,\text{atmos}}^{-1} + (\tau_{t,\text{sfc}}^{-1} - \tau_{t,\text{atmos}}^{-1}) \left(\frac{\sigma(p, p_{\text{sfc}}) - \sigma_{\text{top}}}{1 - \sigma_{\text{top}}}\right) \cos^4(\phi) & \sigma_{\text{top}} \leq \sigma \leq 1 \end{cases}$$

$$T_{\text{eq}}(\phi, p) = \max \left\{ \left[T_0 - (\Delta\Theta)_{\text{h,eq}} \sin^2 \phi - (\Delta\Theta)_{\text{v,eq}} \cos^2 \phi \log \left(\frac{p}{p_0} \right) \right] \left(\frac{p}{p_0} \right)^\kappa, T_{\text{strat}} \right\}$$

where τ_t is the *thermal damping timescale*, T_{eq} is the equilibrium temperature, $\tau_{t,\text{sfc}}$ is the maximum thermal damping timescale (realized at the surface on the equator), $\tau_{t,\text{atmos}}$ is the free-troposphere thermal damping timescale, $(\Delta\Theta)_{\text{h,eq}}$ is the equilibrium equator-pole surface temperature difference, $(\Delta\Theta)_{\text{v,eq}}$ controls the static stability of the equilibrium temperature field, p_0 is the reference pressure 1000hPa, and κ is Poisson’s constant. Damping is stronger in the boundary layer to inhibit the formation of unrealistically strong boundary layer inversions (cf. HS94).

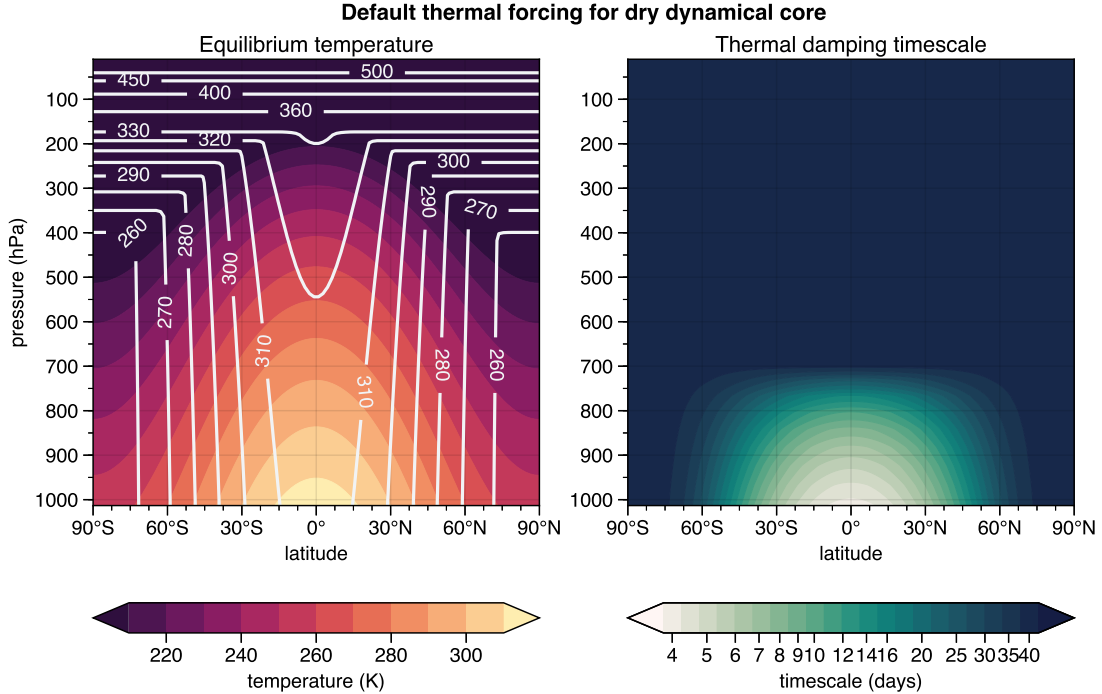


Figure 3.1: (left, shading) The equilibrium temperature, (left, contours) equilibrium potential temperature, and (right) thermal damping timescales for the HS94 configuration of the dry dynamical core. See text for details.

3.3 Experiments

As described in section 1.3, we want to systematically modify the thermal damping parameterization to understand how diabatic heating and climate sensitivity (see subsection 2.2.2) influence the extratropical circulation. To do so, we carried out a series of *parameter sweep* experiments. The experiments are itemized and discussed in detail below; see Table 3.2 for a brief summary of each experiment.

KATMOS: For these experiments, we changed the free-atmosphere damping timescale $\tau_{t,\text{atmos}}$. The timescales were spaced roughly logarithmically: 0.2, 0.4, 1, 2, 4, 10, 20, 40, 100, 200, 400, and 1000 days. Note that 40 days is the HS94 default.

Changing $\tau_{t,\text{atmos}}$ requires scaling the boundary layer damping, which is not spatially uniform under HS94. We considered two scaling approaches, termed KATMOS1 and KATMOS2:

KATMOS1: The damping timescale is held constant throughout the entire atmosphere. With this configuration, the “local” climate sensitivity is everywhere constant (see subsection 2.2.3).

KATMOS2: The minimum boundary-layer timescale $\tau_{t,\text{sfc}}$ is scaled to preserve the HS94 ratio $\tau_{t,\text{atmos}}/\tau_{t,\text{sfc}} = 10$. This mirrors the approach of Z08.

In our discussion, we will focus on the *KATMOS1 experiments*, due to 1) its simpler relationship with climate sensitivity, and 2) issues with double-jet formation for longer-timescale KATMOS2 experiments. When the free-atmosphere damping timescale is very weak, wave generation is disproportionately favored in the subtropical boundary layer, where diabatic heating rates are strong enough to support persistent eddy heat fluxes. This leaves enough “space” in the extratropics for a secondary baroclinic zone to form – ordinarily, double-jet formation is inhibited by large eddy length scales and the geometry of the sphere. The KATMOS1 experiments indeed produce strong surface inversions, but this does not affect our conclusions.

KATMOS-MEAN For these experiments, we first re-wrote the diabatic heating equation Equation 3.4 as in Z08 and Zurita-Gotor et al. (2013) [73]:

$$\begin{aligned} \left(\frac{dT}{dt}\right)_t &= -\tau_t^{-1}(\phi, p) \left[T^*(\lambda, \phi, p, t) + \bar{T}(\phi, p, t) - T_{\text{eq}}(\phi, p) \right] \\ &= -\tau_t^{*-1}(\phi, p) T^*(\lambda, \phi, p, t) - \bar{\tau}_t^{-1}(\phi, p) \left[\bar{T}(\phi, p, t) - T_{\text{eq}}(\phi, p) \right] \end{aligned} \quad (3.5)$$

where τ_t^* is the damping timescale for zonal anomalies in temperature, $\bar{\tau}_t$ is the damping timescale for the zonal mean temperature. Note that $\tau_t^{-1} = \tau_t^{*-1} = \bar{\tau}_t^{-1}$ in the standard configuration.

We then changed the mean damping component $\bar{\tau}_t$ while holding τ_t^* constant at the HS94 value of 40 days, selecting the timescales 4, 10, 20, 40, 100, 200, 400, and 1000 days. The model became numerically unstable with timescales faster than 4 days, since

the background/equilibrium state is baroclinically unstable; by this point, eddy fluxes cannot act quickly enough to restore the background to a stable configuration.

These experiments were intended remove the direct impact of thermal damping on eddy growth processes, which becomes relevant once the damping rate approaches the Eady theory-predicted maximum growth rate for baroclinic waves (Eady (1949) [21]; Figure 3.2). Note also that by construction, the zonal average of heating acting upon the temperature anomalies is zero. Therefore, the component of damping acting on the anomalies has no effect on the climate sensitivity; τ may be replaced with $\bar{\tau}$ in Equation 2.3.

For the **KATMOS1-MEAN** and **KATMOS2-MEAN** variations, the mean boundary layer damping component was changed as in KATMOS1 and KATMOS2.

TGRAD: For this experiment, we varied the equilibrium equator-pole surface temperature difference $(\Delta\Theta)_{h,eq}$ linearly from 20K to 160K in steps of 20K. Note that 60K is the HS94 default.

The TGRAD experiment was meant as a point of comparison for the KATMOS and KATMOS-MEAN thermal damping experiments. The thermal damping experiments change the climate sensitivity of the atmosphere, but they also modify the background state by encouraging larger temperature gradients with stronger damping. Since equilibrium temperature does not affect climate sensitivity, any circulation response *unique* to the thermal damping experiments must directly result from changes to the climate sensitivity, rather than changes to the background meridional temperature gradient.

For thermal damping timescales shorter than 40 days, we used “cold starts” (i.e. an isothermal initial state). For longer timescales, we used “warm starts” (i.e. an initial state equivalent to the final state of the model run with the next-fastest timescale). A global Lorenz energy budget analysis (not shown) suggested the warm starts reduced the necessary “spinup” time from as much as 2000 days to below 500 days. In all cases, we found a timestep

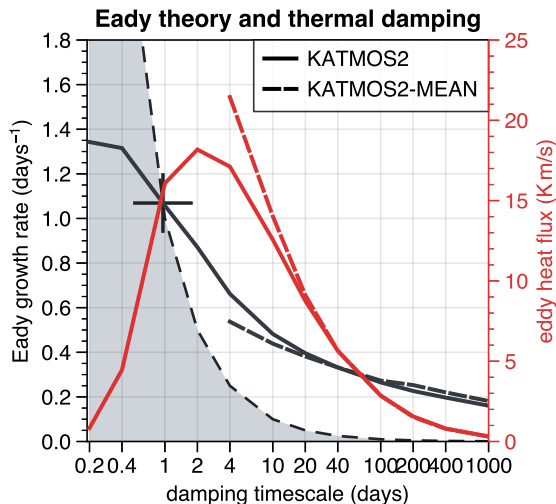


Figure 3.2: (left, black) Eady growth rate averaged between latitudes 20-70°, pressures 1000-500hPa; (right, red) eddy heat flux averaged over the same region. Solid lines (thick dashed lines) correspond to experiments where the full damping rate (zonal-mean damping rate) was changed. Gray shading indicates where the thermal damping rate (i.e. the inverse thermal damping timescale) is greater than the Eady growth rate. The plus sign indicates where the KATMOS2 experiment series crosses this threshold.

of 1200s was sufficient to satisfy the Courant-Friedrichs-Lewy or “CFL” condition (Courant et al., 1928 [19]).

For each run, we used the 12-hourly instantaneous output from 5500-day integrations of the model. The first 500 days were omitted to account for model “spinup.” Prior to each analysis, the model output was linearly interpolated from hybrid coordinates (see Equation 3.1) to isobaric (constant pressure) or isentropic (constant potential temperature) coordinates. We handled sub-surface potential temperature surfaces as in Held and Schneider (1999) [35] – that is, we set sub-surface “pressure” to the surface pressure, and sub-surface “geopotential height” to the surface geopotential height (zero, since the model has no topography).

For the climatological analyses, since the forcing scheme is equinoctial (i.e. the hemispheres have equivalent statistical equilibria), we averaged the northern and southern hemispheres. This has the added benefit of doubling the “effective” integration time (assuming negligible cross-equatorial flow).

Table 3.2: Description and naming conventions for the various experiment series. See text for further details.

Experiment name	Parameter(s) changed	HS94 value	Boundary layer scaling
KATMOS1	$\tau_{t,\text{atmos}}$	40 days	$\tau_{t,\text{sfc}} = \tau_{t,\text{atmos}}$
KATMOS2	"	"	$\tau_{t,\text{atmos}}/\tau_{t,\text{sfc}} = 10$
KATMOS1-MEAN	$\bar{\tau}_{t,\text{atmos}}$	"	$\bar{\tau}_{t,\text{sfc}} = \bar{\tau}_{t,\text{atmos}}$
KATMOS2-MEAN	"	"	$\bar{\tau}_{t,\text{atmos}}/\bar{\tau}_{t,\text{sfc}} = 10$
TGRAD	$(\Delta\Theta)_{\text{h,eq}}$	60K	Not applicable

Chapter 4

Results

In this chapter, we summarize results from the KATMOS, KATMOS-MEAN, and TGRAD parameter sweep experiments (see section 3.3, Table 3.2), paying particular attention to the KATMOS-MEAN experiments.

4.1 Overview

Figure 4.1 shows the climatological diabatic heating (shading) and potential temperature (contours) from the KATMOS-MEAN and TGRAD experiments, respectively. Under stronger thermal damping (top-left direction), the extratropical cooling rates significantly increase, especially near the tropopause, while the zone of diabatic boundary-layer heating intensifies.

These observations are summarized in Figure 4.2, in which the experiments are compared relative to $\Delta\Theta_h$. We define $\Delta\Theta_h$ as the difference between the average temperature over 0°-10° latitude and 70°-90° latitude – it is a bulk measure of the extratropical meridional temperature gradient, and a convenient metric for inter-comparison. Note that, as indicated by the legend, solid lines correspond to the TGRAD, KATMOS2, and KATMOS2-MEAN experiments, while the dashed lines correspond to the KATMOS1 and KATMOS1-MEAN experiments; see Table 3.2.

We see that stronger equilibrium temperature gradients lead to *larger* deviations from equilibrium, while stronger damping leads to *smaller* deviations from equilibrium (left panel). Furthermore, the damping timescale appears to have a much stronger influence on diabatic heating than the equilibrium temperature (middle, right panels).

From Figure 4.3, we see that stronger damping corresponds to stronger eddy heat fluxes (see scales at bottom-left of each panel). This is unsurprising if we consider the steady-state solution to the thermodynamic equation (Equation 2.1): Stronger diabatic heating rates

Diabatic heating in KATMOS1-MEAN experiments

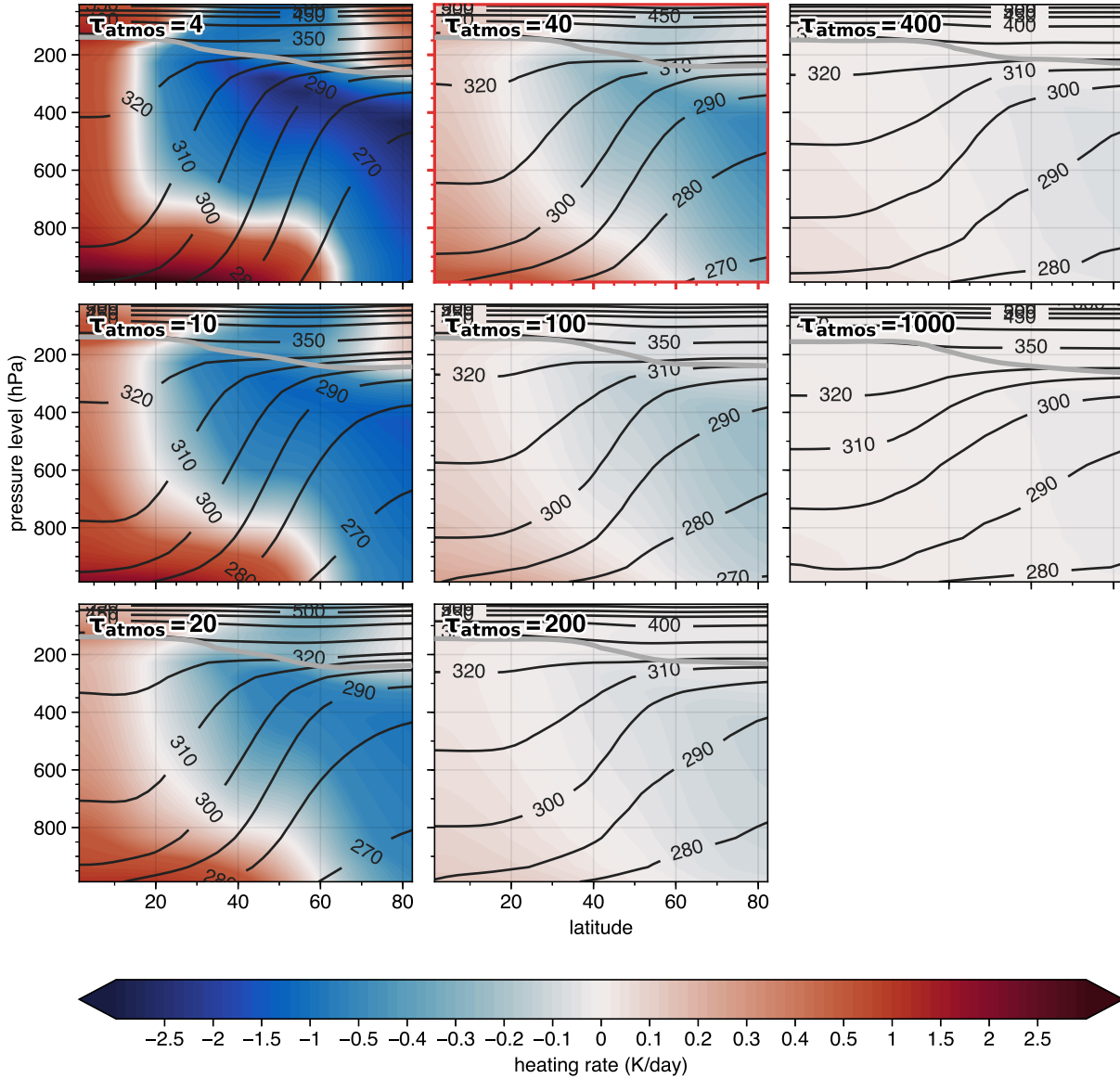


Figure 4.1: (shading) Zonal-mean diabatic heating rates and (contours, units K) potential temperature for the ATOMS-MEAN parameter sweep. Note that the heating rate scale is non-linear. The gray contour indicates the AMS tropopause (i.e. the lowest level with 2K/km vertical lapse rate). Each panel represents the average of the southern and northern hemisphere 5000-day climatologies. The thermal damping timescales are increasing from top-left to bottom-right in column-major order, and are indicated in the top-left corner of each plot. The panel outlined in red indicates the HS94 value of 40 days.

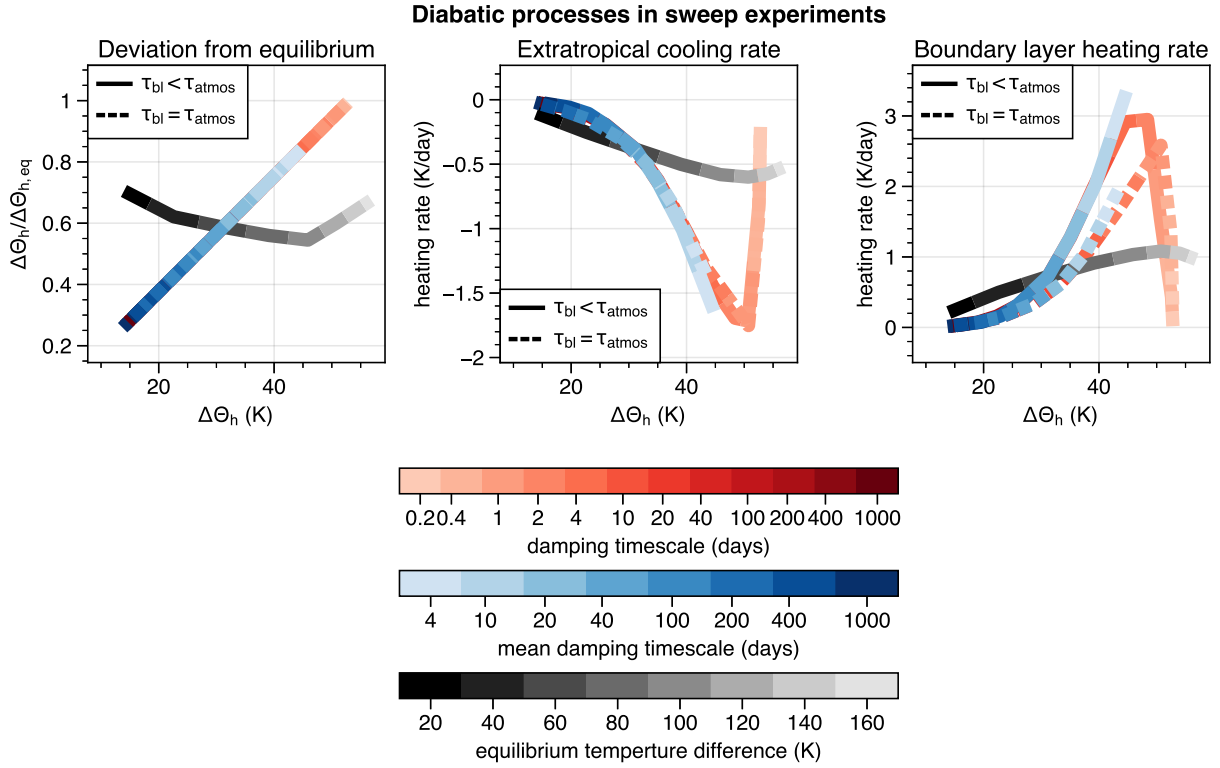


Figure 4.2: Parametric depictions of diabatic heating across the parameter sweep experiments. The colors red, blue, and gray correspond to the KATMOS, KATMOS-MEAN, and TGRAD experiments, respectively. Each colored “block” corresponds to an individual 5000-day climatology. As indicated by the legend, dashed red/blue lines correspond to the KATMOS1 and KATMOS1-MEAN experiments (in which damping is constant throughout the atmosphere), and solid red/blue lines correspond to the KATMOS2 and KATMOS2-MEAN experiments (in which the boundary layer damping is stronger); see Table 3.2 for details. The following metrics are plotted relative to the bulk horizontal temperature difference $\Delta\Theta_h$ (see text): (left) the ratio of the equilibrium equator-pole temperature difference $\Delta\Theta_{h,eq}$ to $\Delta\Theta_h$; (middle) the average extratropical cooling rate over 50° - 90° latitude and 850-250hPa; and (right) the average boundary layer heating rate over 10° - 40° latitude and 1000-850hPa.

must be balanced by stronger heat fluxes and adiabatic heating – in essence, an invigoration of the extratropical circulation. Interestingly, Figure 4.3 also shows that strong damping considerably *expands* the meridional extent of the largest heat fluxes. This may imply the damping timescale affects the prevalence of an extratropical “storm track” (e.g. Hoskins and Valdes (1989) [39]).

We also see that the slope of the potential temperature contours in Figure 4.3 seem to *increase* with stronger damping. Figure 4.4 summarizes these changes using a “bulk” measure of *isentropic slope* $\Delta\Theta_h/\Delta\Theta_v - \Delta\Theta_h$ is defined as before, and $\Delta\Theta_v$ is defined as the difference between the average surface temperature and tropopause potential temperature between 20°-70° latitude. Under constant isentropic slope, we expect each line in the *top-left panel* to follow the thin dashed black line – which is more-or-less true for the TGRAD experiment, but not at all true for the KATMOS experiments. The same can be inferred from the top-right panel of Figure 4.4, which depicts bulk isentropic slope $\Delta\Theta_h/\Delta\Theta_v$ against $\Delta\Theta_h$. Thus, baroclinic adjustment theory (or the “constant criticality” constraint; cf. Stone (1978) [67]) is violated for the KATMOS experiments. This makes sense if we consider that with stronger damping, the temperature is everywhere drawn closer to the “equilibrium” state, which itself is characterized by extremely steep isentropic slopes.

Another common assumption in understanding extratropical dynamics is “constant diffusivity” – that eddy fluxes of temperature are proportional to the background gradient across which they flow (i.e. $v^*T^*/\partial_y\bar{T}$ is a constant). Figure 4.4 shows this too is violated for the KATMOS experiments. The dashed black line in the bottom panel represents constant diffusivity relative to the HS94 configuration. It is roughly followed by the TGRAD experiments, but not the KATMOS experiments. The diffusivity collapses to zero for the KATMOS1 and KATMOS2 experiments when thermal damping becomes strong enough to prohibit the growth of individual eddies.

We also find that stronger damping is associated with stronger downgradient potential vorticity fluxes, both in the boundary layer and in the free troposphere (Figure 4.5, shading).

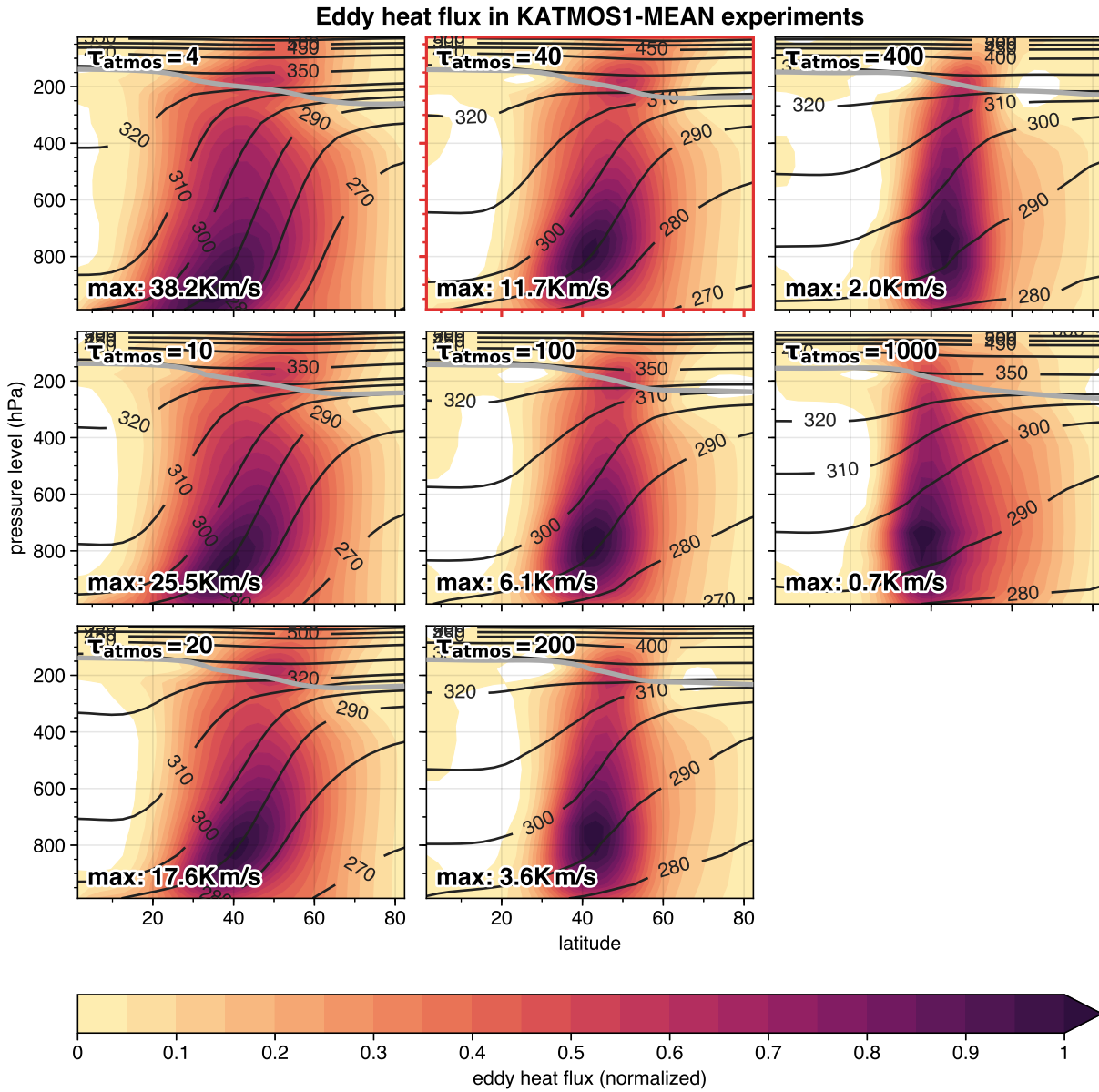


Figure 4.3: As in Figure 4.1, but for the eddy heat flux (shading) and isentropic slope (contours, units m/km). This time, the color scales in each panel are normalized by the values indicated at the bottom-left.

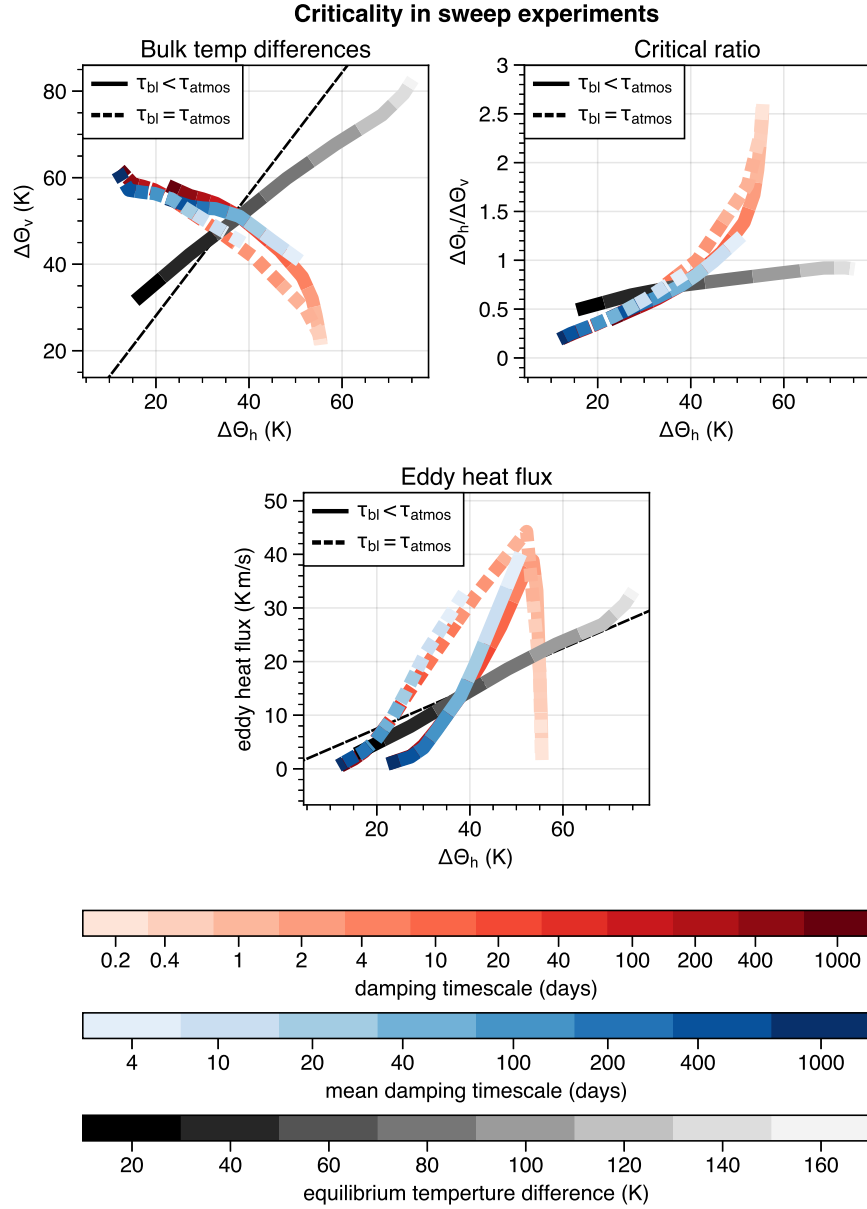


Figure 4.4: As in Figure 4.2, but comparing $\Delta\Theta_h$ against (top-left) the bulk surface-tropopause potential temperature difference $\Delta\Theta_v$; (top-right) the ratio $\Delta\Theta_h/\Delta\Theta_v$; and (bottom) the maximum eddy heat flux averaged between 1000hPa and 500hPa. Dashed black lines indicate (top-left) constant criticality and (bottom) constant diffusivity.

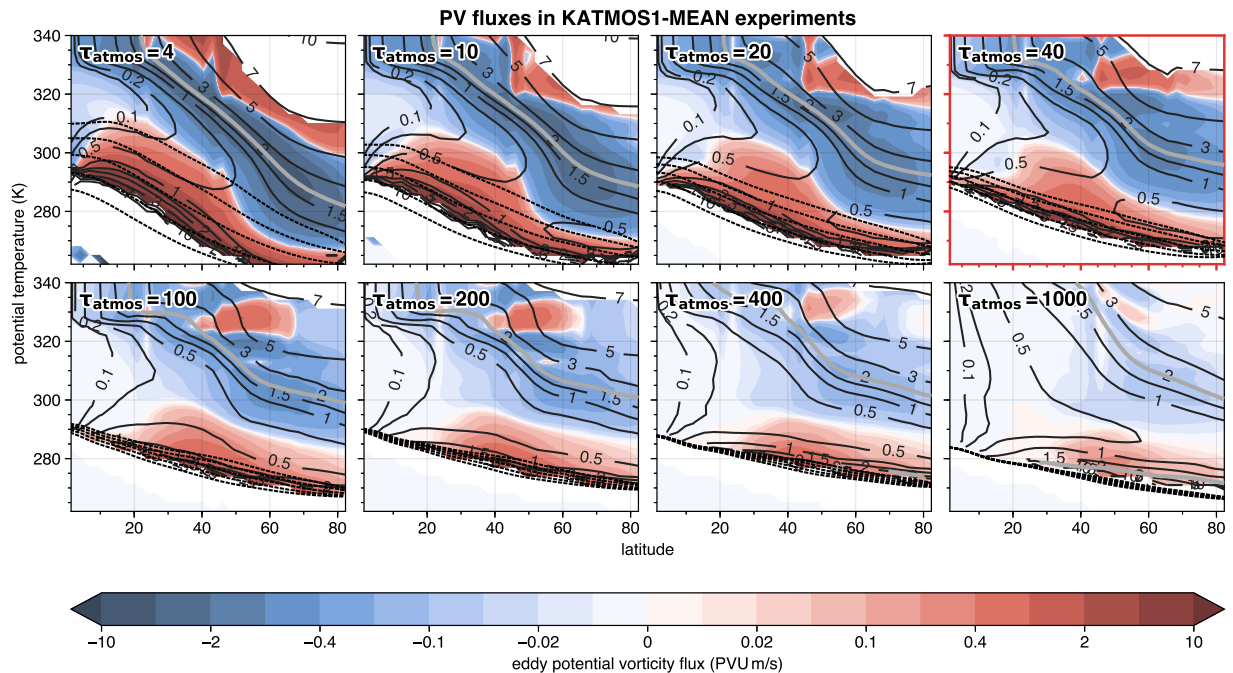


Figure 4.5: As in Figure 4.1, but showing eddy potential vorticity fluxes (shading) and zonal-mean potential vorticity (contours, units PVU) in *isentropic* coordinates. This time the solid gray contour indicates the 2PVU “dynamical” tropopause. The thin, dashed contours indicate the 5th, 20th, 50th, 80th, and 95th percentile surface potential temperatures.

The dashed black lines indicate the range of 5th to 95 percentile surface potential temperatures, and are also suggestive of extremely high near-surface temperature variance and strong eddy heat fluxes, consistent with Figure 4.3.

Figure 4.6 depicts the global energy storage and energy flow terms in the format of an energy-flow diagram (e.g. Oort (1964) [53]) for the KATMOS2-MEAN and TGRAD experiments as a function of $\Delta\Theta_h$. The energy cycle terms are defined in section A.1. As expected, stronger damping and larger equilibrium temperature gradients tend to intensify of the energy cycle – and changing the thermal damping timescale (blue lines) leads to a more “efficient” intensification with respect to the meridional temperature gradient. Figure 4.7 replicates this figure, but with the mean extratropical diabatic cooling rate (averaged between 1000hPa and 200hPa, 50°-90° latitude) on the x -axis. Evidently, extratropical diabatic cooling is superior in predicting the strength of the energy cycle than the meridional

temperature gradient. This is perhaps self-evident – if the magnitude of the diabatic heating term in the thermodynamic equation grows, the magnitude of the dynamical terms must change in kind. A notable difference is the dissociation of mean-flow kinetic energy from diabatic cooling for large equilibrium temperature differences in the TGRAD experiment (red box, top-right). This dissociation is also imprinted on the adjacent conversion and dissipation terms (black boxes). This may result from an intensified barotropic component of zonal-mean zonal wind. While the relative strength of the barotropic and baroclinic eddies does not seem to change much for the KATMOS experiments, this ratio may indeed change with the TGRAD experiments.

Eddy-mean Lorenz energy cycle, relative to meridional temperature gradients

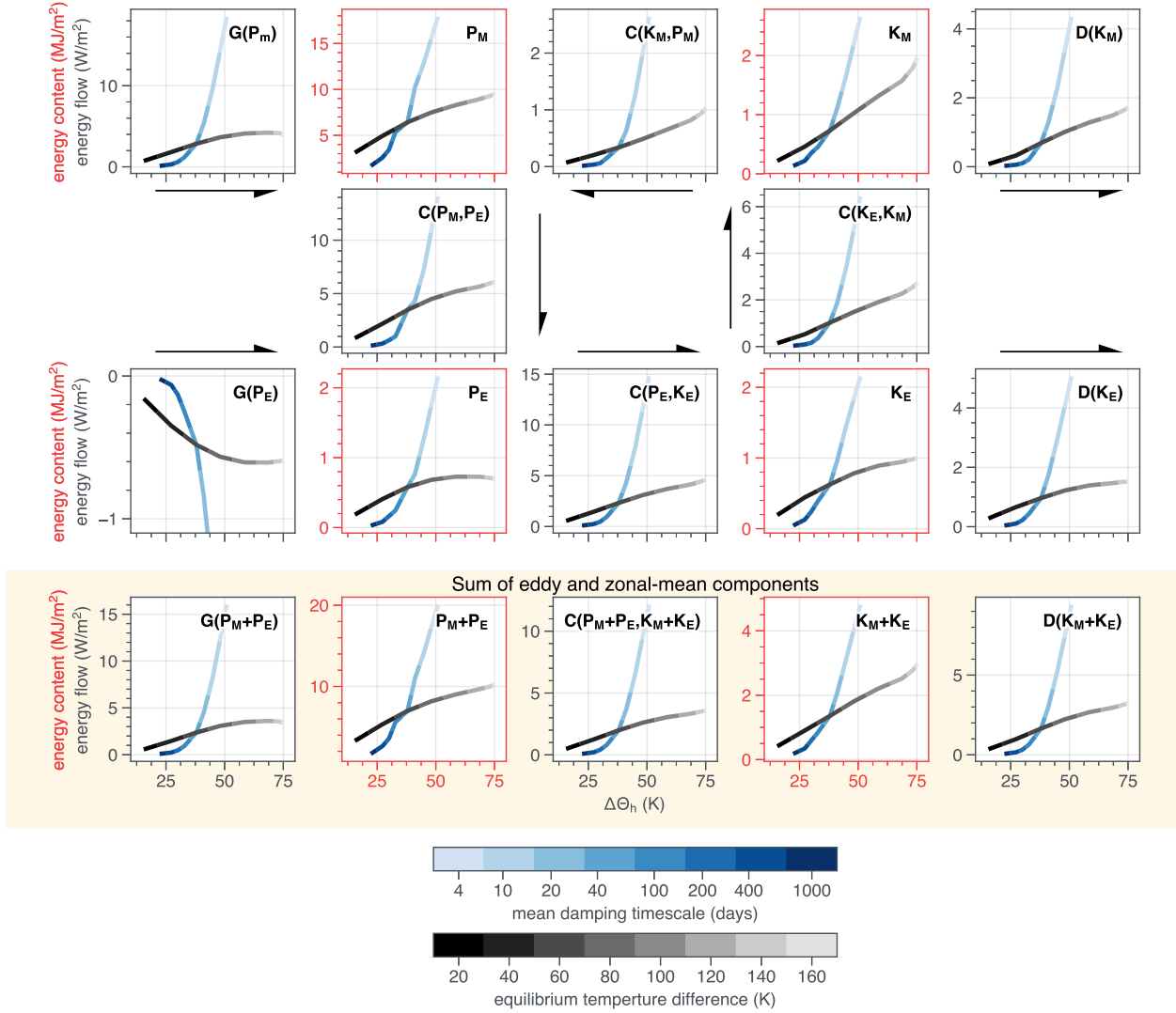


Figure 4.6: Lorenz energy budget terms for the different sweep experiments, as a function of the bulk meridional temperature gradient $\Delta\Theta_h$. Boxes in red indicate energy content terms (units MJ m^{-2}), and boxes in gray indicate energy transfer terms (units W m^{-2}). From left-to-right, the top row shows (1) the mean (diabatic) generation of available potential energy (APE); (2) the mean APE; (3) the conversion from mean kinetic energy to mean APE; (4) the mean kinetic energy; and (5) the frictional dissipation of mean kinetic energy. The third row is as in the first row, but for the eddy components, and with the conversion term positive in the direction of potential-kinetic energy conversion. The second row shows conversion from (left) mean APE to eddy APE, and (right) eddy kinetic energy to mean kinetic energy. The bottom row shows the sum of the eddy and mean components of APE generation, APE, APE-kinetic energy conversion, kinetic energy, and dissipation of kinetic energy. The notation in the top-right corner of each panel matches Oort (1964) [53].

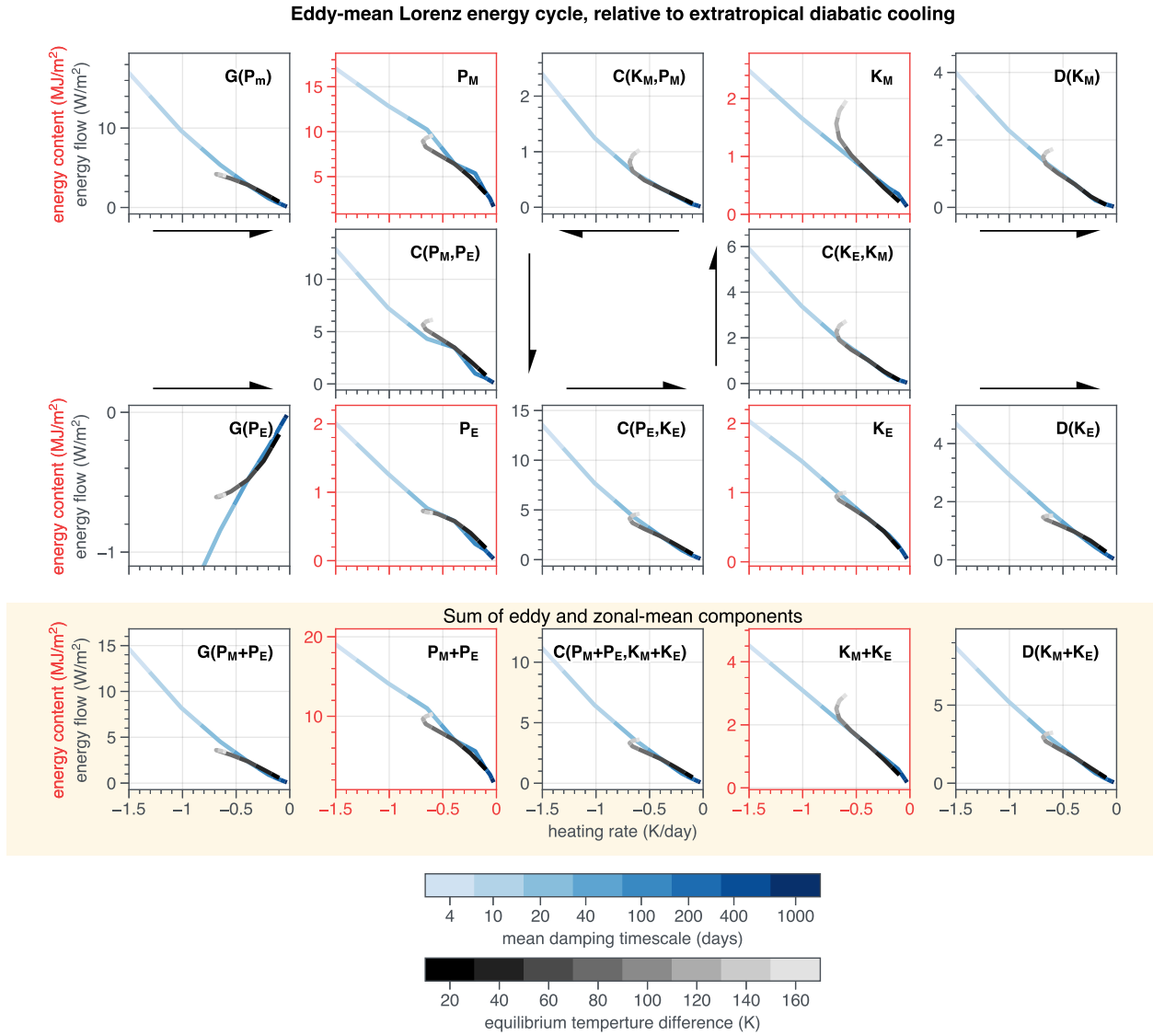


Figure 4.7: As in Figure 4.6, but with the extratropical diabatic cooling rates on the x -axis. The cooling rates were averaged over 50° - 90° latitude, 400-800hPa.

4.2 Wave driving and propagation

Next, we take a closer look at wave characteristics across the sweep experiments. Figure 4.8 depicts the climatological Eliassen-Palm (EP) flux. We define the Eliassen-Palm flux \vec{F} as

$$\vec{F} \equiv \left(-\cos \phi \overline{u^*v^*}, \quad f \cos \phi \frac{\overline{v^*T^*}}{\partial \theta / \partial p} \right)$$

where ϕ is the latitude, u the zonal wind, v the meridional wind, T the temperature, θ the potential temperature, f the Coriolis parameter, p the pressure, and the asterisks denote a zonal anomaly (i.e. a deviation from the zonal mean). The divergence of the EP flux is found with

$$\nabla \cdot \vec{F} \equiv \frac{1}{\cos \phi} \frac{\partial (F_y \cos \phi)}{\partial \phi} + \frac{\partial F_z}{\partial z}$$

In Figure 4.8, positive shading indicates EP flux divergence (i.e. **wave generation**), negative shading EP flux convergence (i.e. **wave breaking** or **wave drag**), and arrows the direction of wave propagation (scaled as in Andrews (1987) [2]).

With stronger damping, we see that wave generation near the extratropical surface intensifies and expands meridionally. Further, wave breaking aloft seems to grow relatively stronger compared to wave generation. This is likely due to an intensification of the barotropic component of the flow, which would not impact near-surface wave generation. Stronger damping also tends to draw the wave breaking region *upward and equatorward*; weak damping favors the *decoupling* of the thermodynamic tropopause and the extratropical dynamics, consistent with the analysis shown in Figure 4.9. Figure 4.9 shows the average subtropical tropopause height between 10°-40° latitude according to the (left) thermodynamic and (right) “mass transport” definitions. The latter corresponds to the height at which the residual mass streamfunction reaches 10% of its maximum value (cf. Schneider (2004) [59]) – that is, 90% of poleward mass transport occurs below this level. The thermodynamic tropopause appears to be stable across all experiments, while the mass transport-defined tropopause descends considerably over longer timescales.

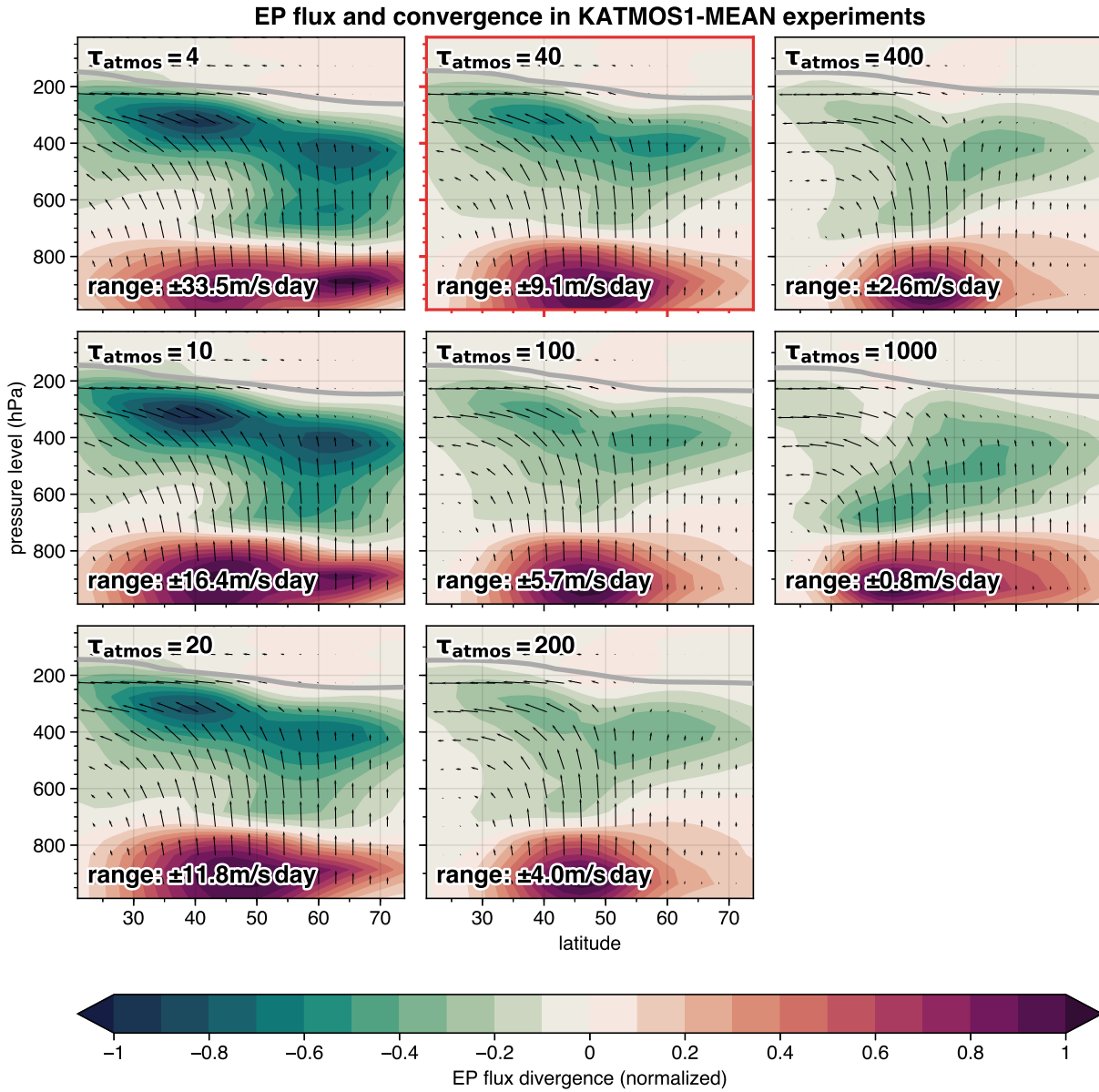


Figure 4.8: As in Figure 4.1, but for the EP flux divergence (shading) and components of the EP flux vectors (arrows). The scaling is as in Andrews (1987) [2].

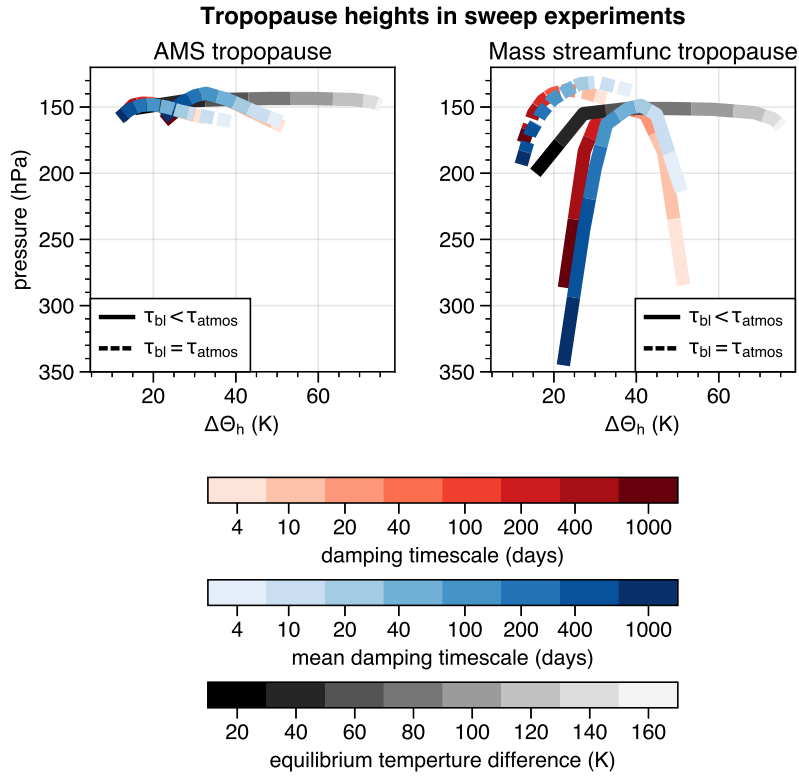


Figure 4.9: As in Figure 4.2, but showing averages over 10° - 40° latitude of the pressure levels for the (left) thermodynamic tropopause (i.e. the $2\text{K}/\text{km}$ lapse rate) and (right) the mass transport-defined tropopause (i.e. the height at which the residual mass streamfunction reaches 10% of its maximum value).

Figure 4.10 summarizes changes to the wave driving length scales (i.e. length scales associated with 500hPa EP-flux divergence co-spectra) for the KATMOS2, KATMOS2-MEAN, and TGRAD experiments. For methods, see section A.2. We immediately see that the stronger the damping, the larger the eddy length scales. The same goes for the equilibrium temperature gradient, but in this case, the magnitude of the response is much weaker.

The panels in Figure 4.10 show 3 metrics used for predicting eddy length scales from the zonal-mean background state:

1. The Rossby radius of deformation L_d , a measure of the maximum length scale limited by differential rotation of the Earth, i.e. the β -effect. L_d is defined $L_d \equiv NH/f_0$, where H is the characteristic height of the troposphere, N the static stability, and f_0 a characteristic Coriolis parameter.
2. The Rhines- β scale L_R , a measure of the length scale to which the inverse energy cascade is limited, owing to potential vorticity conservation. L_R is defined $L_R \equiv \sqrt{2|v^*|/\beta_0}$, where $|v^*|$ is the root-mean-square zonal meridional wind anomaly and β_0 is a characteristic β -parameter ($\beta \equiv \partial f/\partial y$)
3. The eddy displacement scale L_{disp} , a measure of the *diffusivity* of the flow. L_{disp} is defined as in Barry et al. (2002) [9]: $L_{\text{disp}} \equiv |T^*|/(\partial T/\partial y)$, where $|T^*|$ is the root-mean-squared zonal temperature anomaly and $\partial T/\partial y$ the meridional temperature gradient.

We see that for the TGRAD experiments, the eddy length scale is a function of the Rossby deformation radius (bottom-left), owing to the corresponding static-stability changes (top-left). For the KATMOS experiments, the length scales actually *increase* as the deformation radii decrease. The Rhines- β scale (top-right) is evidently a superior predictor of the eddy-length scales, in that it at least grows larger as the damping strength increases. However, the scaling is imperfect for all experiments, and is again the least accurate for the KATMOS experiments. The displacement-length scale plot (bottom-right) confirms that diffusivity is a poor predictor of extratropical eddy activity, as suggested by Figure 4.4.

Finally, we show the phase-speed spectra of 500hPa EP-flux divergence for the KATMOS2-MEAN experiments in Figure 4.11. For methods, see section A.2. As expected from thermal wind, stronger damping tends to expand the region of wave propagation, intensify the wave breaking, and increase the eddy phase speeds. In particular, stronger damping tends to intensify and expand the wave breaking region on the equatorward flank of the jet. This is consistent with the poleward motion of the eddy-driven jet under stronger damping rates, as discussed in the next section.

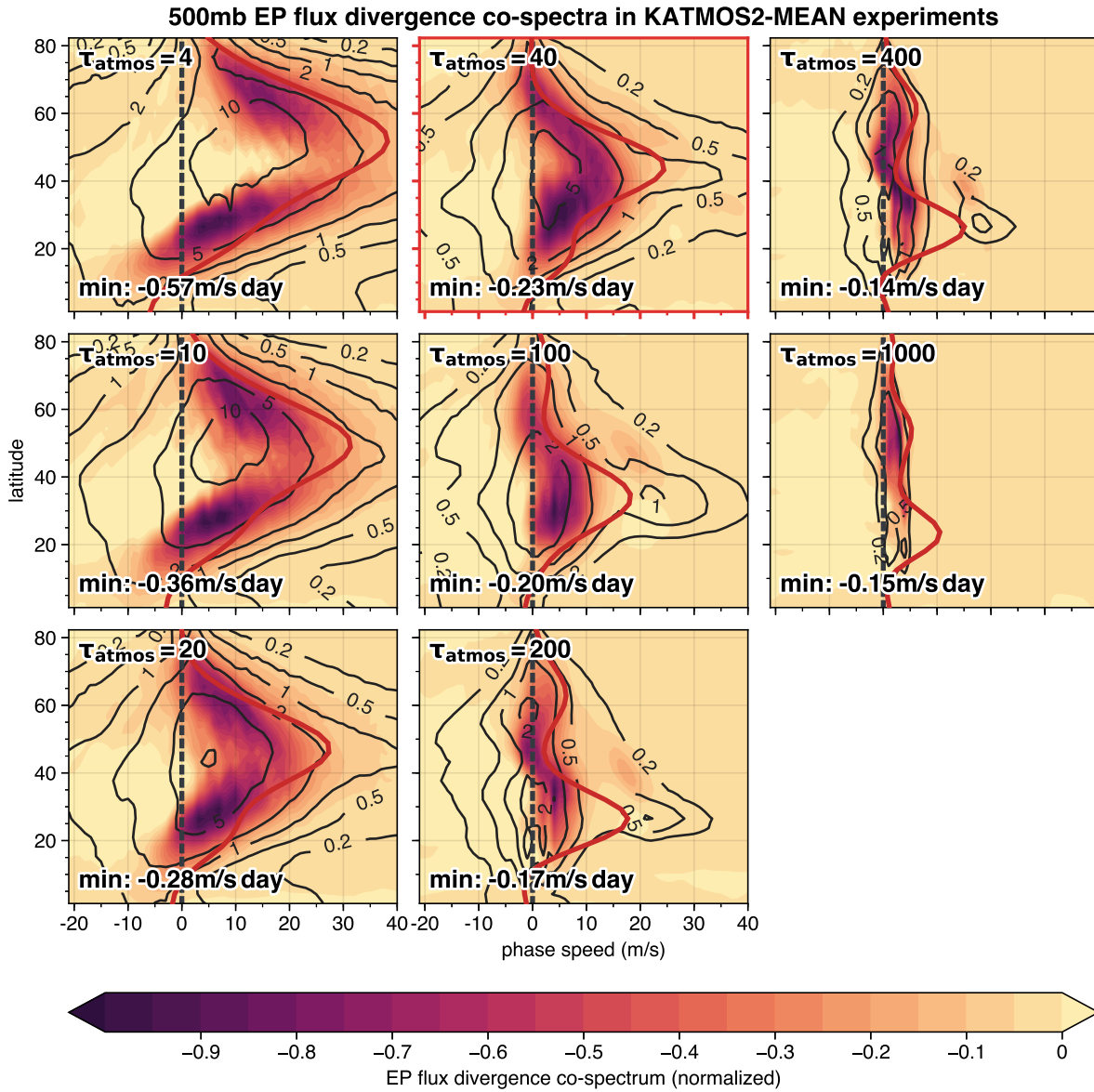


Figure 4.11: As in Figure 4.3, but instead showing the (shading) co-spectral power of the 500hPa Eliassen-Palm (EP) flux divergence and (contours, units m^2/s^2) spectral power of the 500hPa meridional wind anomalies as a function of phase speed (x -axis) and latitude (y -axis). The red contour indicates the 500hPa zonal-mean zonal wind.

4.3 Subtropical and eddy-driven jets

We also examined how the subtropical and eddy-driven jets changed in the sweep experiments. Figure 4.12 depicts the eddy momentum flux convergence (shading) and the zonal-mean zonal wind (contours) for the KATMOS2-MEAN runs. We see that stronger damping corresponds to a more intense and higher-latitude eddy-driven jet. This relationship between eddy strength and jet latitude is thought to be a simple consequence of spherical geometry, as suggested by Barnes and Hartmann (2011) [8] and confirmed by our experiments. The doubled-jet formation with weak damping is another indication of the twin baroclinic zones, present in the KATMOS2 experiments and absent in the KATMOS1 experiments (see section 3.3). In the KATMOS2-MEAN experiment, the jet moves equatorward in part because the relatively stronger damping found in the subtropical boundary layer can sustain stronger eddy heat fluxes. As this is perhaps more an artifact of the forcing scheme than a physically meaningful result, we return our attention to the KATMOS1-MEAN experiment.

Figure 4.13 shows how various indicators of the (red) eddy-driven jet and (blue) subtropical jet change across the KATMOS1-MEAN and TGRAD experiments. The results are quite similar – with weak meridional temperature gradients (i.e. small $\bar{\tau}_t$, large $(\Delta\Theta)_{h,eq}$), the eddy-driven jet is drawn equatorward and *merges* with the subtropical jet.

Figure 4.14 shows the relationship between the strength of the eddy-forcing of the extratropical jet and the latitude of the eddy-driven jet (i.e. the red lines in the left and right panels of Figure 4.13). We find that the relationship is roughly *identical* for the KATMOS2-MEAN and TGRAD experiments – larger eddy-momentum flux convergence corresponds to a more poleward jet. Again, this is supportive of the spherical geometry mechanism described by Barnes and Hartmann (2011) [8]; diabatic forcing does not seem to change this relationship. We also notice there appears to be a *maximum eddy-driven jet latitude* of between 50° - 55° for every experiment, at which point eddy fluxes may continue to strengthen, but the jet will no longer move poleward. We suspect a similar geometric argument may explain this phenomenon.

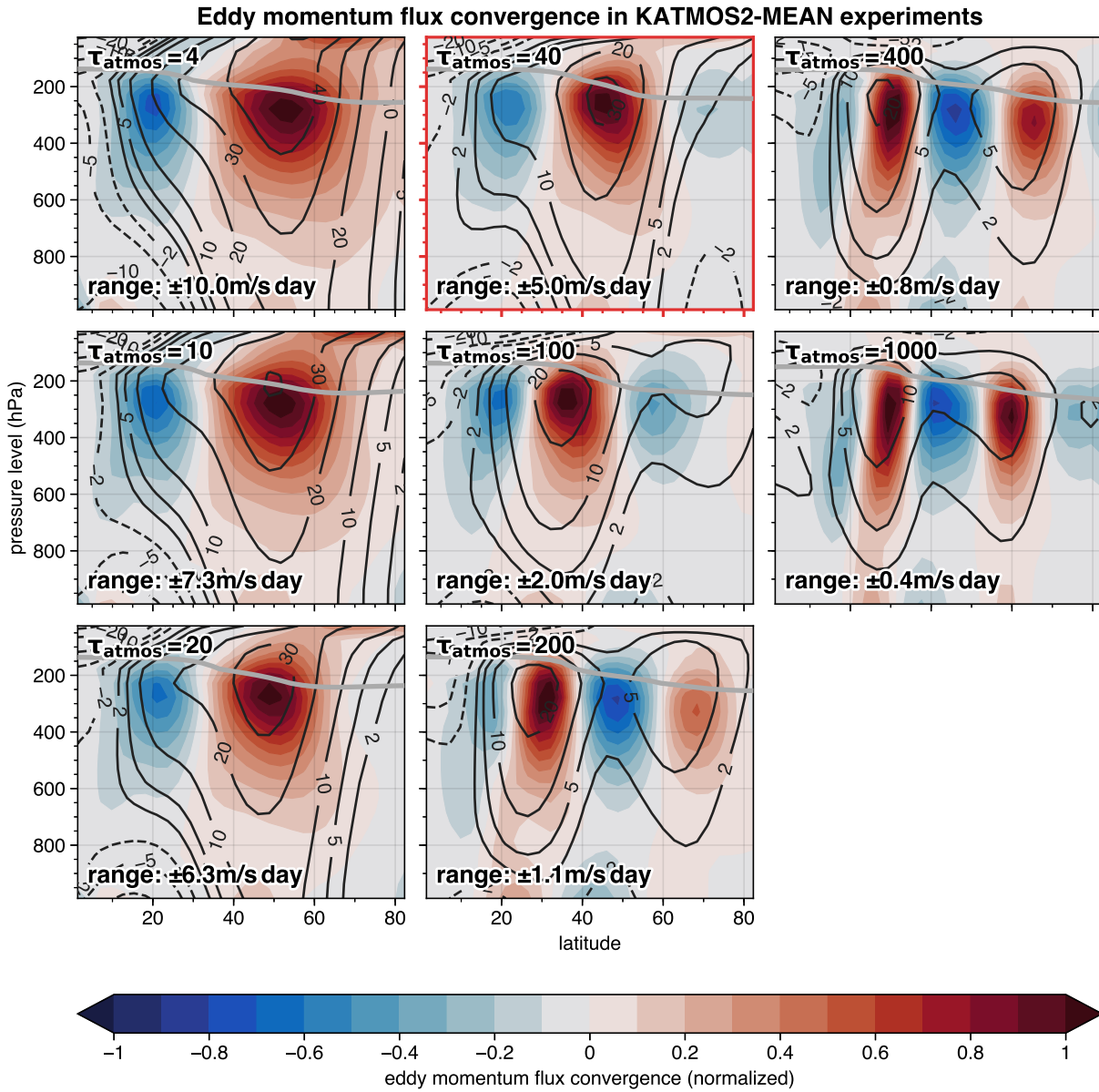


Figure 4.12: As in Figure 4.3, but for the (shading) eddy momentum flux convergence and (contours, units m/s) zonal-mean zonal wind in the KATMOS2-MEAN experiment.

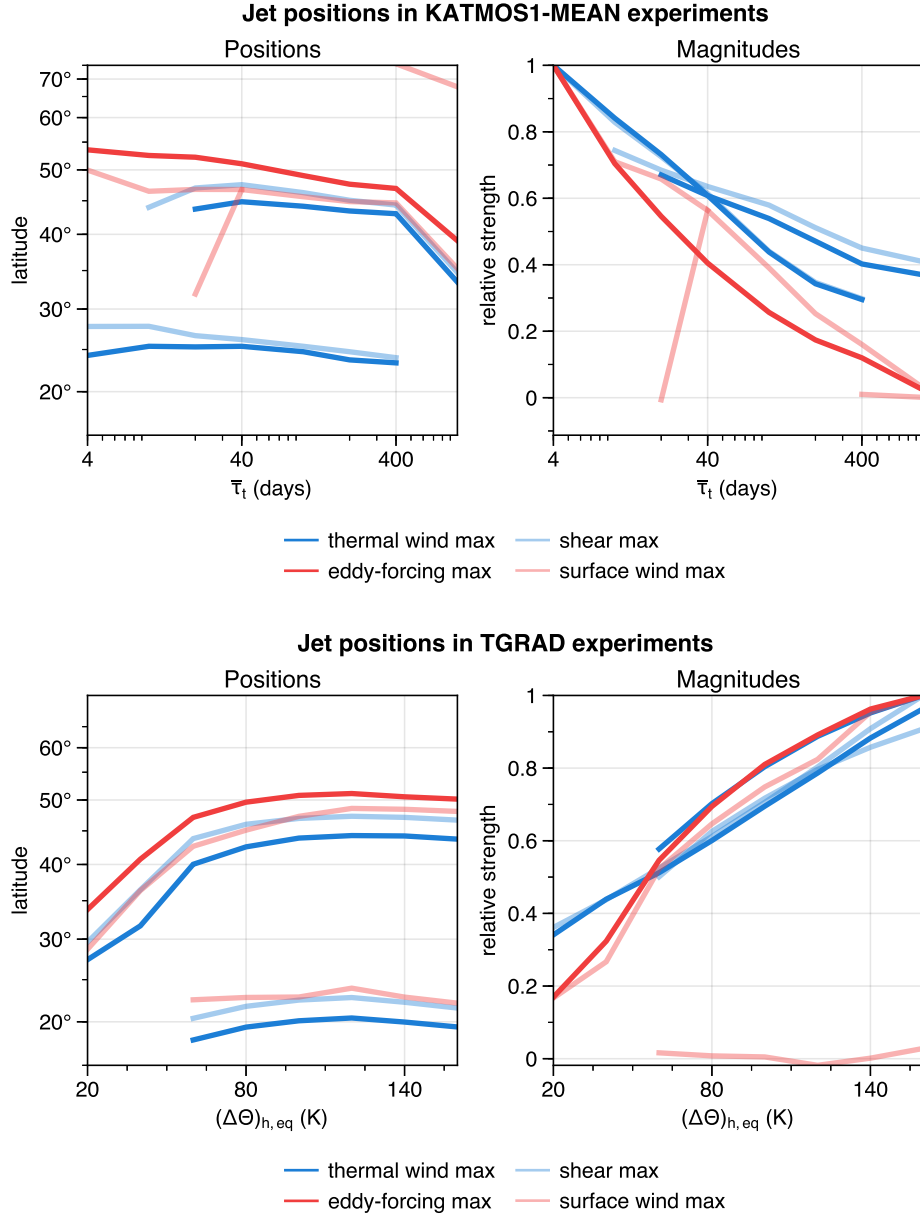


Figure 4.13: Jet stream analysis for the (top) KATMOS1-MEAN and (bottom) TGRAD experiments. Red lines correspond to the eddy-driven jet, detected from (solid red) local maxima in eddy-momentum flux convergence forcing and (pale red) surface wind maxima. Blue lines correspond to the subtropical jet, detected from (solid blue) local maxima in vertically-averaged thermal wind and (pale blue) maxima in vertically averaged shear. Left panels show *latitudes* of the maxima across the experiment climatologies. Right panels show the normalized *strengths* of these maxima. The *x*-axes correspond to the forcing parameter ($\bar{\tau}_t$ for KATMOS1-MEAN, $\Delta\Theta_{h,eq}$ for TGRAD). For a single experiment (i.e. a single point on the *x*-axis), multiple lines indicate the presence of multiple jets.

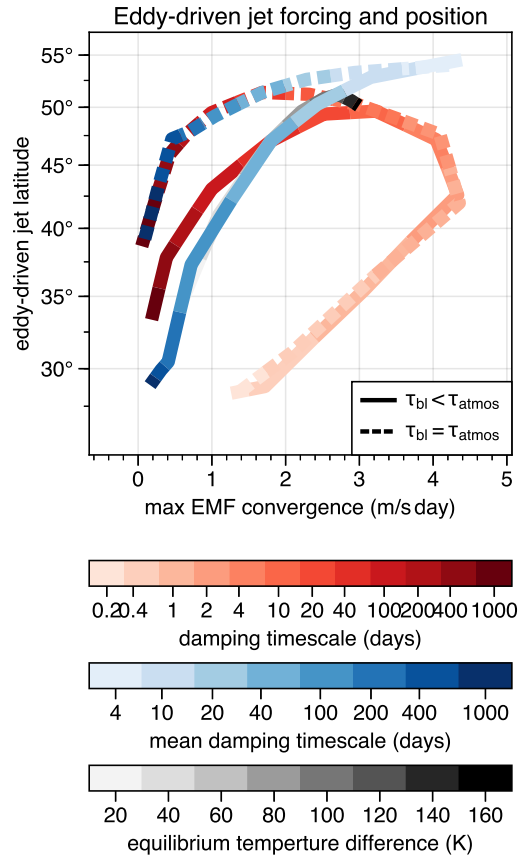


Figure 4.14: As in Figure 4.2, but comparing the latitude of the eddy-driven jet (defined as the latitude of maximum integrated eddy-momentum flux convergence) to the strength of the maximum eddy-momentum flux convergence.

4.4 Climate variability and eddy-mean feedbacks

In our final analysis, we examine the internal climate variability associated with the barotropic annular mode or “SAM” (the first empirical orthogonal function (EOF) of the mean-flow kinetic energy) and the baroclinic annular mode or “BAM” (the first EOF of the eddy kinetic energy), as defined in Thompson and Li (2014) [68]. For methods, see section A.3.

As an example, Figure 4.15 shows the projection of eddy kinetic energy onto the standardized principle component (PC) time series associated with the first and second EOFs of eddy kinetic energy. The first EOF (shading) characterizes the pulsating zonal-average strength of the extratropical storms, and the second EOF (contours) characterizes persistent changes to the latitude of the storm track region. We can see that, while strong damping substantially increases the total variance associated with each mode of variability (for the first EOF, see inset text at bottom of each panel; for the second EOF, see contour labels), the structure of each mode is largely unchanged. Note that the sign of the anomalies is not physically meaningful – rather, the relative structure and strength of the anomalies is important.

We next examine the relative variance explained by the annular modes. Figure 4.16 shows the variance in mean kinetic energy and eddy kinetic energy explained by the SAM and BAM, respectively (top row), as well as the variance in the *forcing fields* explained by the forcing patterns associated with each annular mode (bottom row; see section A.3). From the KATMOS experiments, we see that weaker thermal damping rates tend to **increase** the proportion of variance in the fields themselves (top row) and in the forcing fields (bottom row) explained by the annular modes. This tendency is much weaker for the TGRAD experiments. The tendency for the TGRAD and KATMOS2 experiments to have reduced variance explained with weak meridional temperature gradients is likely, once again, a signature of twin baroclinic zones (see section 3.3). With multiple baroclinic zones, annular variability may be split between the zones or otherwise poorly captured by the EOF analysis procedure.

The KATMOS1 experiments, by comparison, bear a **monotonic** relationship between the damping timescale and variance explained by the annular modes.

Finally, we examined the decorrelation timescales of the annular modes. Results from the KATMOS experiments are shown by Figure 4.17. The decorrelation timescales (or autocorrelation timescales if you prefer) were defined as the least-squares fit to the e -folding time associated with the pure red noise autocorrelation function

$$\rho(N\Delta t) \equiv \exp(-N\rho_0)$$

where $t \equiv N\Delta t$ the time, N is the number of timesteps, Δt is the timestep, and ρ_0 is the lag-1 (i.e. the single-timestep) autocorrelation. We find that the decorrelation timescales significantly increase with weaker thermal damping for both the SAM *and* the BAM.

We see that for the KATMOS1 experiments (left), both the SAM and BAM decorrelation timescales increase with the damping timescale. Above the HS94 default of 40 days, the relationship appears to be nearly **linear**. The similarity of the curves for the BAM and SAM is also striking – both annular modes appear to have the same functional relationship with the thermal damping timescale.

Note that we plan to reproduce the annular mode analyses with a higher resolution configuration of the dry dynamical core. Given the known sensitivity of T42 truncation to the annular mode timescale (Gerber et al. (2008) [27]), we want to ensure our results are robust to model resolution. Although, given the consistency of the relationship between the thermal damping timescale and the annular mode timescales across the 4 variations of the KATMOS experiments, we are optimistic that the results will be largely similar.

"BAM" in KATMOS1-MEAN experiments

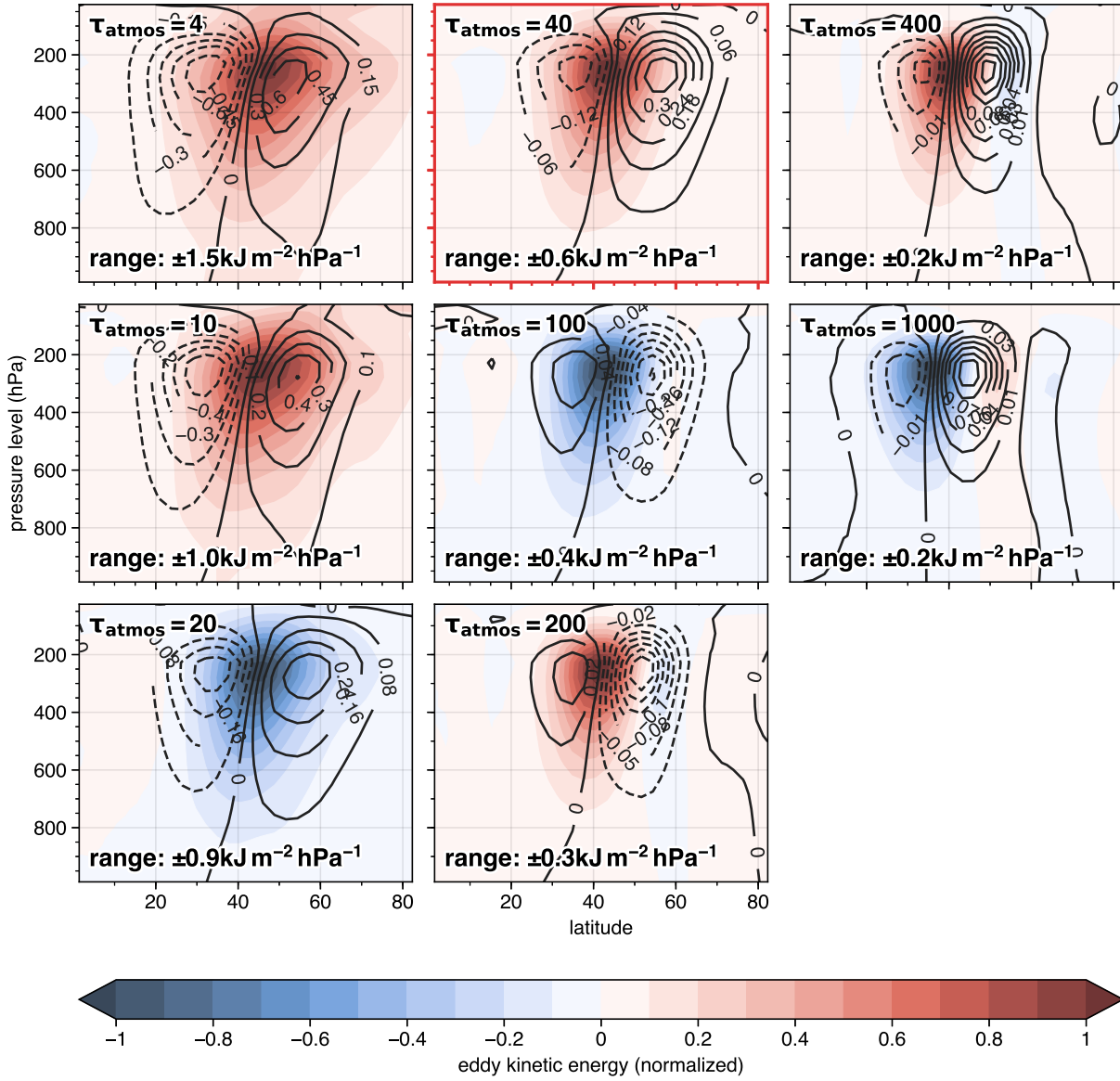


Figure 4.15: As in Figure 4.3, but showing the (shading) first and (contours) second EOFs of eddy kinetic energy.

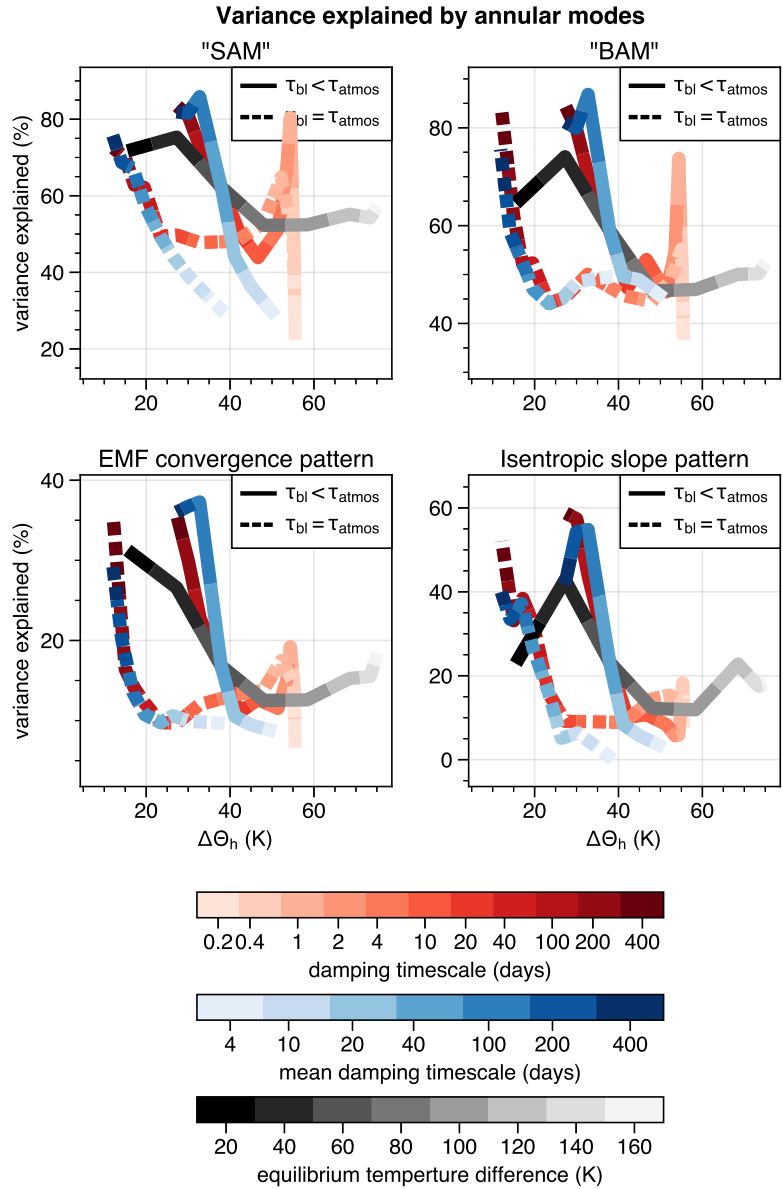


Figure 4.16: As in Figure 4.2, but showing the percent variance explained by the annular modes as a function of the bulk meridional temperature gradient $\Delta\Theta_h$. The top row shows the variance explained by the SAM and BAM in their respective fields (mean kinetic energy and eddy kinetic energy), and the bottom row shows the variance in eddy momentum flux convergence and isentropic slope explained by the *forcing patterns* associated with the annular modes in the top row. See section A.3 for details.

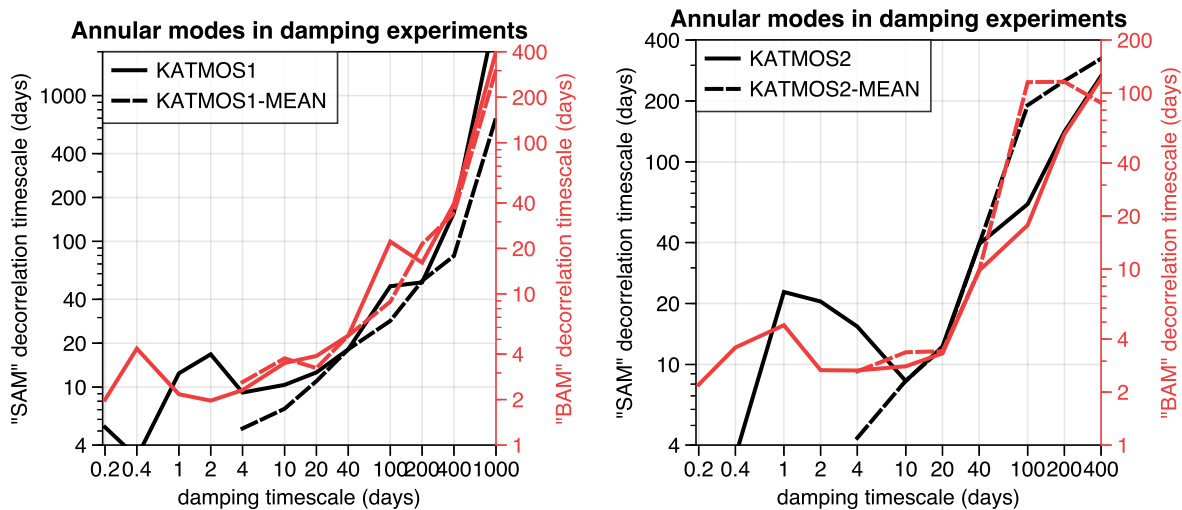


Figure 4.17: Autocorrelation timescales for the annular modes in the (left) KATMOS1 and KATMOS1-MEAN experiments, and (right) KATMOS2 and KATMOS2-MEAN experiments, as a function of the damping timescale τ_t . The black lines (left y -axes) indicate the SAM timescales, and the red lines (right y -axes) indicate the BAM timescales.

Chapter 5

Discussion

5.1 Review

In chapter 3, we described a set of four “parameter sweep” experiments used to perturb the damping timescale in the dry dynamical core: KATMOS1, KATMOS2, KATMOS1-MEAN, and KATMOS2-MEAN. For the “1” experiments, the damping timescale was held constant everywhere (i.e. was not increased in the tropical boundary layer), resulting in a simpler relationship with climate sensitivity and preventing the formation of twin baroclinic zones. For the “2” experiments, the damping timescale was increased in the tropical boundary layer to prevent unrealistically strong inversions from forming. For the “MEAN” experiments, only the component of the damping rate acting on zonal-mean temperature was varied, preventing any interaction between damping and eddy formation processes. These experiments were meant as individually justifiable, but not necessarily “superior” approaches to varying the damping timescale over a wide range of magnitudes. We carried out the “TGRAD” experiment (where the equilibrium temperature gradient was systematically varied) as a point of comparison for the KATMOS experiments, to see whether any circulation changes observed with the KATMOS experiments could be reproduced by changing the equilibrium temperature instead of the damping timescale.

In chapter 3, we showed that the thermal damping timescale in the dry dynamical core is closely related to the global equilibrium climate sensitivity. In the case of the KATMOS1 experiments, the equilibrium climate sensitivity is even a *constant multiple* of this timescale. Thus, any circulation response observed in the KATMOS experiments that was not observed in the TGRAD experiment is likely to be uniquely associated with the climate sensitivity of the dry atmosphere.

In chapter 4, we provided a systematic description of the extratropical circulation changes associated with the KATMOS sweeps. The most salient result was the *invigoration* of the extratropical circulation with stronger thermal damping. That is, stronger thermal damping lead to an intensification of the eddy fluxes of heat and potential vorticity (Figure 4.3, Figure 4.5), growth of the Lorenz energy cycle reservoirs and strengthening of the transport terms (Figure 4.6), and strengthening of the residual mass overturning circulation. These observations more-or-less corroborated the results from Zurita-Gotor (2008) [72].

We also found that near-surface wave generation intensified with stronger damping (Figure 4.8), that eddy length scales and phase speeds increased (Figure 4.10), and that the atmospheric channel suitable for wave propagation expanded (Figure 4.11). Stronger damping favored increased eddy momentum fluxes (Figure 4.12) with associated poleward motion of the eddy-driven jet (Figure 4.13), revealing an apparent “maximum” latitude of around 50° for the eddy-driven jet in the dry atmosphere. Finally, stronger damping favored relatively weaker (Figure 4.16) and shorter-timescale (Figure 4.17) annular modes.

5.2 Conclusions

It is remarkable that the majority of extratropical responses we observed were, more than anything else, a function of *net diabatic heating*. That is whether the damping timescale or equilibrium temperature was changed to produce a particular diabatic heating climatology, the extratropical circulation looked roughly the same. This is perhaps unsurprising, given that the atmospheric dynamics are most fundamentally coupled to the thermodynamic equation by the diabatic heating as a whole. But it also may point to the difficulty of using steady-state climate to estimate the climate sensitivity of the atmosphere, no matter the functional form of its diabatic heating.

Nevertheless, the TGRAD experiment failed to reproduce a small minority of circulation changes associated with the KATMOS experiments – implying these features may be uniquely associated with climate sensitivity. These changes are summarized as follows:

- The isentropic slope increases with the thermal damping rate, but is roughly unchanged when the equilibrium temperature is changed. *The constant criticality constraint is violated when the thermal damping timescale is changed.*
- The autocorrelation timescales and variance explained by the barotropic and baroclinic annular modes decrease significantly as the thermal damping rate increases. *The eddy-mean flow feedback mechanism seems to be inhibited by strong damping rates.*
- The region of eddy fluxes and baroclinic wave generation tends to expand as the damping rate increases, but contract as the equilibrium temperature gradient increases. *Stronger damping tends to make the “storm rack” region wider.*

It may be possible to use these features – local or global isentropic slope, annular mode timescale, or storm track breadth – as *proxies* for climate sensitivity. That is, these features could be used to estimate the climate sensitivity for a dry atmosphere with unknown “damping timescale.” By identifying consistent relationships between the circulation and the climate sensitivity, we hope they may be used to better understand and predict climate sensitivity in the real world.

5.3 Future work

In this thesis, we have discussed the “climate sensitivity” of the dry atmosphere at length. But so far, we have only considered how climate sensitivity affects the steady-state climate and unforced climate variability in the dry atmosphere. While this may be useful for estimating climate sensitivity from the unforced state of an atmosphere, it would also be interesting to see this configurable “climate sensitivity” in action – that is, to see the circulation *response* to “global warming” is affected by climate sensitivity.

As such, we plan to carry out “global warming” experiments with the dry dynamical core. This can be done by holding the thermal damping timescale fixed, then simulating global warming in one of two ways:

1. Systematically changing the global mean equilibrium temperature and/or the equilibrium equator-pole temperature gradient.
2. Adding a constant heating term to the thermodynamic equation.

The former represents an “interactive” heating that can feed back with the dynamical terms in the thermodynamic equation. The latter represents a “non-interactive” heating that to some degree fixes the other terms in the thermodynamic equation. Whichever is more appropriate, this would be an extremely simple way to simulate the circulation response to global warming – and therefore, this could help us understand the circulation response to global warming in more complex climate models, like those belonging to the Coupled-Model Intercomparison Project (CMIP5; e.g. Andrews et al., 2012 [5]).

We would also like to study how the circulation response to *local* climate-change like thermal forcings (e.g. those used by Butler et al., 2010 [15]) is affected by “climate sensitivity.” Butler et al. (2010) [15] showed that any circulation response can largely be explained by the projection of the local heating anomaly onto the isentropic slope. Since we found that the morphology and intensity of isentropic slope was dependent on climate sensitivity, we suspect that changing the damping timescale may have a *substantial* impact on the circulation response.

It is notable in of itself that, for the dry atmosphere, climate sensitivity is governed by the same diabatic mechanism that governs internal climate variability. With this in mind, it may be possible to infer the thermal damping timescale from the autocorrelation function for the diabatic heating rate. If this proves possible for the dry atmosphere, we would like to try a similar analysis for the fully-coupled CMIP5 models. By coming up with an “effective damping timescale” for the CMIP5 models, we may be able to “predict” their response to global warming – which we can easily compare to the empirically diagnosed climate sensitivity from the CMIP5 $2\times\text{CO}_2$ experiments.

Bibliography

- Andrews, D. G. (1983), ‘A Finite-Amplitude Eliassen-Palm Theorem in Isentropic Coordinates’, *Journal of the Atmospheric Sciences* **40**(8), 1877–1883.
- Andrews, D. G. (1987), ‘On the interpretation of the Eliassen-palm flux divergence’, *Quarterly Journal of the Royal Meteorological Society* **113**(475), 323–338.
- Andrews, D. G., Leovy, C. B. and Holton, J. R. (1987), *Middle Atmosphere Dynamics*, Academic Press.
- Andrews, D. G. and McIntyre, M. E. (1976), ‘Planetary Waves in Horizontal and Vertical Shear: The Generalized Eliassen-Palm Relation and the Mean Zonal Acceleration’, *Journal of the Atmospheric Sciences* **33**(11), 2031–2048.
- Andrews, T., Gregory, J. M., Webb, M. J. and Taylor, K. E. (2012), ‘Forcing, feedbacks and climate sensitivity in CMIP5 coupled atmosphere-ocean climate models’, *Geophysical Research Letters* **39**(9).
- Armour, K. C., Bitz, C. M. and Roe, G. H. (2012), ‘Time-Varying Climate Sensitivity from Regional Feedbacks’, *Journal of Climate* **26**(13), 4518–4534.
- Baker, H. S., Woollings, T. and Mbengue, C. (2017), ‘Eddy-Driven Jet Sensitivity to Diabatic Heating in an Idealized GCM’, *Journal of Climate* **30**(16), 6413–6431.
- Barnes, E. A. and Hartmann, D. L. (2011), ‘Rossby Wave Scales, Propagation, and the Variability of Eddy-Driven Jets’, *Journal of the Atmospheric Sciences* **68**(12), 2893–2908.
- Barry, L., Craig, G. C. and Thuburn, J. (2002), ‘Poleward heat transport by the atmospheric heat engine’, *Nature* **415**(6873), 774–777.
- Bell, T. L. (1980), ‘Climate Sensitivity from Fluctuation Dissipation: Some Simple Model Tests’, *Journal of the Atmospheric Sciences* **37**(8), 1700–1707.

- Boljka, L. and Shepherd, T. G. (2018), ‘A Multiscale Asymptotic Theory of Extratropical Wave–Mean Flow Interaction’, *Journal of the Atmospheric Sciences* **75**(6), 1833–1852.
- Boljka, L., Shepherd, T. G. and Blackburn, M. (2018), ‘On the Coupling between Barotropic and Baroclinic Modes of Extratropical Atmospheric Variability’, *Journal of the Atmospheric Sciences* **75**(6), 1853–1871.
- Brayshaw, D. J., Hoskins, B. and Blackburn, M. (2008), ‘The Storm-Track Response to Idealized SST Perturbations in an Aquaplanet GCM’, *Journal of the Atmospheric Sciences* **65**(9), 2842–2860.
- Butler, A. H., Thompson, D. W. J. and Birner, T. (2011), ‘Isentropic Slopes, Downgradient Eddy Fluxes, and the Extratropical Atmospheric Circulation Response to Tropical Tropospheric Heating’, *Journal of the Atmospheric Sciences* **68**(10), 2292–2305.
- Butler, A. H., Thompson, D. W. J. and Heikes, R. (2010), ‘The Steady-State Atmospheric Circulation Response to Climate Change–like Thermal Forcings in a Simple General Circulation Model’, *Journal of Climate* **23**(13), 3474–3496.
- Chen, G., Held, I. M. and Robinson, W. A. (2007), ‘Sensitivity of the Latitude of the Surface Westerlies to Surface Friction’, *Journal of the Atmospheric Sciences* **64**(8), 2899–2915.
- Chen Gang and Held Isaac M. (2007), ‘Phase speed spectra and the recent poleward shift of Southern Hemisphere surface westerlies’, *Geophysical Research Letters* **34**(21).
- Cionni, I., Visconti, G. and Sassi, F. (2004), ‘Fluctuation dissipation theorem in a general circulation model’, *Geophysical Research Letters* **31**(9).
- Courant, R., Friedrichs, K. and Lewy, H. (1928), ‘Über die partiellen Differenzgleichungen der mathematischen Physik’, *Mathematische Annalen* **100**(1), 32–74.
- Dee, D. P., Uppala, S. M., Simmons, A. J., Berrisford, P., Poli, P., Kobayashi, S., Andrae, U., Balmaseda, M. A., Balsamo, G., Bauer, P., Bechtold, P., Beljaars, A. C. M., van de

- Berg, L., Bidlot, J., Bormann, N., Delsol, C., Dragani, R., Fuentes, M., Geer, A. J., Haimberger, L., Healy, S. B., Hersbach, H., Hólm, E. V., Isaksen, I., Kållberg, P., Köhler, M., Matricardi, M., McNally, A. P., Monge-Sanz, B. M., Morcrette, J.-J., Park, B.-K., Peubey, C., de Rosnay, P., Tavolato, C., Thépaut, J.-N. and Vitart, F. (2011), ‘The ERA-Interim reanalysis: Configuration and performance of the data assimilation system’, *Quarterly Journal of the Royal Meteorological Society* **137**(656), 553–597.
- Eady, E. T. (1949), ‘Long Waves and Cyclone Waves’, *Tellus* **1**(3), 33–52.
- Feldstein, S. and Lee, S. (1998), ‘Is the Atmospheric Zonal Index Driven by an Eddy Feedback?’, *Journal of the Atmospheric Sciences* **55**(19), 3077–3086.
- Frankignoul, C. (1985), ‘Sea surface temperature anomalies, planetary waves, and air-sea feedback in the middle latitudes’, *Reviews of Geophysics* **23**(4), 357–390.
- Frankignoul, C., Czaja, A. and L’Heveder, B. (1998), ‘Air–Sea Feedback in the North Atlantic and Surface Boundary Conditions for Ocean Models’, *Journal of Climate* **11**(9), 2310–2324.
- Frierson, D. M. W. (2008), ‘Midlatitude Static Stability in Simple and Comprehensive General Circulation Models’, *Journal of the Atmospheric Sciences* **65**(3), 1049–1062.
- Gerber, E. P. and Vallis, G. K. (2007), ‘Eddy–Zonal Flow Interactions and the Persistence of the Zonal Index’, *Journal of the Atmospheric Sciences* **64**(9), 3296–3311.
- Gerber, E. P., Voronin, S. and Polvani, L. M. (2008), ‘Testing the Annular Mode Autocorrelation Time Scale in Simple Atmospheric General Circulation Models’, *Monthly Weather Review* **136**(4), 1523–1536.
- Gritsun, A. and Branstator, G. (2007), ‘Climate Response Using a Three-Dimensional Operator Based on the Fluctuation–Dissipation Theorem’, *Journal of the Atmospheric Sciences* **64**(7), 2558–2575.

- Gritsun, A., Branstator, G. and Majda, A. (2008), ‘Climate Response of Linear and Quadratic Functionals Using the Fluctuation–Dissipation Theorem’, *Journal of the Atmospheric Sciences* **65**(9), 2824–2841.
- Hansen, J., Lacis, A., Rind, D., Russell, G., Stone, P., Fung, I., Ruedy, R. and Lerner, J. (1984), Climate Sensitivity: Analysis of Feedback Mechanisms, *in* ‘Climate Processes and Climate Sensitivity’, American Geophysical Union (AGU), pp. 130–163.
- Hansen, J., Russell, G., Lacis, A., Fung, I., Rind, D. and Stone, P. (1985), ‘Climate Response Times: Dependence on Climate Sensitivity and Ocean Mixing’, *Science* **229**(4716), 857–859.
- Hartmann, D. L. and Lo, F. (1998), ‘Wave-Driven Zonal Flow Vacillation in the Southern Hemisphere’, *Journal of the Atmospheric Sciences* **55**(8), 1303–1315.
- Haynes, P., Scinocca, J. and Greenslade, M. (2001), ‘Formation and maintenance of the extratropical tropopause by baroclinic eddies’, *Geophysical Research Letters* **28**(22), 4179–4182.
- Held, I. M. (1999), ‘The macroturbulence of the troposphere’, *Tellus A* **51**(1), 59–70.
- Held, I. M. and Schneider, T. (1999), ‘The Surface Branch of the Zonally Averaged Mass Transport Circulation in the Troposphere’, *Journal of the Atmospheric Sciences* **56**(11), 1688–1697.
- Held, I. M. and Soden, B. J. (2006), ‘Robust Responses of the Hydrological Cycle to Global Warming’, *Journal of Climate* **19**(21), 5686–5699.
- Held, I. M. and Suarez, M. J. (1994), ‘A Proposal for the Intercomparison of the Dynamical Cores of Atmospheric General Circulation Models’, *Bulletin of the American Meteorological Society* **75**(10), 1825–1830.

- Hitchcock, P., Shepherd, T. G. and Yoden, S. (2009), ‘On the Approximation of Local and Linear Radiative Damping in the Middle Atmosphere’, *Journal of the Atmospheric Sciences* **67**(6), 2070–2085.
- Hoskins, B. J. and Valdes, P. J. (1989), ‘On the Existence of Storm-Tracks’, *Journal of the Atmospheric Sciences* **47**(15), 1854–1864.
- Jeevanjee, N., Hassanzadeh, P., Hill, S. and Sheshadri, A. (2017), ‘A perspective on climate model hierarchies’, *Journal of Advances in Modeling Earth Systems* **9**(4), 1760–1771.
- Juckes, M. N. (2000), ‘The Static Stability of the Midlatitude Troposphere: The Relevance of Moisture’, *Journal of the Atmospheric Sciences* **57**(18), 3050–3057.
- Kirtman, B., Power, S., Adedoyin, J., Boer, G., Bojariu, R., Camilloni, I., Doblas-Reyes, F., Fiore, A., Kimoto, M., Meehl, G., Prather, M., Sarr, A., Schafler, C., Sutton, R., van Oldenborgh, G., Vecchi, G. and Wang, H. (2013), *Near-term Climate Change: Projections and Predictability*, Cambridge University Press, Cambridge, United Kingdom and New York, NY, USA, book section 11, p. 953–1028.
- Leith, C. E. (1975), ‘Climate Response and Fluctuation Dissipation’, *Journal of the Atmospheric Sciences* **32**(10), 2022–2026.
- Lorenz, D. J. and Hartmann, D. L. (2001), ‘Eddy–Zonal Flow Feedback in the Southern Hemisphere’, *Journal of the Atmospheric Sciences* **58**(21), 3312–3327.
- Lorenz, E. N. (1955), ‘Available Potential Energy and the Maintenance of the General Circulation’, *Tellus* **7**(2), 157–167.
- Lu, J., Vecchi, G. A. and Reichler, T. (2007), ‘Expansion of the Hadley cell under global warming’, *Geophysical Research Letters* **34**(6).
- Lucarini, V., Fraedrich, K. and Lunkeit, F. (2010), ‘Thermodynamics of Climate Change: Generalized Sensitivities’, *Atmospheric Chemistry and Physics* **10**(20), 9729–9737.

- Manabe, S. and Strickler, R. F. (1964), ‘Thermal Equilibrium of the Atmosphere with a Convective Adjustment’, *Journal of the Atmospheric Sciences* **21**(4), 361–385.
- Mbengue, C. and Schneider, T. (2013), ‘Storm Track Shifts under Climate Change: What Can Be Learned from Large-Scale Dry Dynamics’, *Journal of Climate* **26**(24), 9923–9930.
- Modest, M. F. (2013), *Radiative Heat Transfer*, Academic Press.
- Nakamura, H., Sampe, T., Tanimoto, Y. and Shimpo, A. (2013), Observed Associations Among Storm Tracks, Jet Streams and Midlatitude Oceanic Fronts, *in* ‘Earth’s Climate’, American Geophysical Union (AGU), pp. 329–345.
- Nakamura, N. and Zhu, D. (2010), ‘Finite-Amplitude Wave Activity and Diffusive Flux of Potential Vorticity in Eddy–Mean Flow Interaction’, *Journal of the Atmospheric Sciences* **67**(9), 2701–2716.
- Oort, A. H. (1964), ‘On estimates of the atmospheric energy cycle’, *Monthly Weather Review* **92**(11), 483–493.
- Polvani, L. M. and Kushner, P. J. (2002), ‘Tropospheric response to stratospheric perturbations in a relatively simple general circulation model’, *Geophysical Research Letters* **29**(7), 18–1.
- Randel, W. J. and Held, I. M. (1991), ‘Phase Speed Spectra of Transient Eddy Fluxes and Critical Layer Absorption’, *Journal of the Atmospheric Sciences* **48**(5), 688–697.
- Ring, M. J. and Plumb, R. A. (2007), ‘Forced Annular Mode Patterns in a Simple Atmospheric General Circulation Model’, *Journal of the Atmospheric Sciences* **64**(10), 3611–3626.
- Roe, G. H. and Baker, M. B. (2007), ‘Why Is Climate Sensitivity So Unpredictable?’, *Science* **318**(5850), 629–632.

- Santer, B. D., Wehner, M. F., Wigley, T. M. L., Sausen, R., Meehl, G. A., Taylor, K. E., Ammann, C., Arblaster, J., Washington, W. M., Boyle, J. S. and Brüggemann, W. (2003), ‘Contributions of Anthropogenic and Natural Forcing to Recent Tropopause Height Changes’, *Science* **301**(5632), 479–483.
- Schneider, T. (2004), ‘The Tropopause and the Thermal Stratification in the Extratropics of a Dry Atmosphere’, *Journal of the Atmospheric Sciences* **61**(12), 1317–1340.
- Schneider, T. (2006), ‘The General Circulation of the Atmosphere’, *Annual Review of Earth and Planetary Sciences* **34**(1), 655–688.
- Shaw, T. A., Baldwin, M., Barnes, E. A., Caballero, R., Garfinkel, C. I., Hwang, Y.-T., Li, C., O’Gorman, P. A., Rivière, G., Simpson, I. R. and Voigt, A. (2016), ‘Storm track processes and the opposing influences of climate change’, *Nature Geoscience* **9**(9), 656–664.
- Shepherd, T. G. (2002), ‘Issues in Stratosphere-troposphere Coupling’, *Journal of the Meteorological Society of Japan. Ser. II* **80**(4B), 769–792.
- Simmons, A. J. and Burridge, D. M. (1981), ‘An Energy and Angular-Momentum Conserving Vertical Finite-Difference Scheme and Hybrid Vertical Coordinates’, *Monthly Weather Review* **109**(4), 758–766.
- Simmons, A. J. and Hoskins, B. J. (1978), ‘The Life Cycles of Some Nonlinear Baroclinic Waves’, *Journal of the Atmospheric Sciences* **35**(3), 414–432.
- Small, R. J., deSzoeko, S. P., Xie, S. P., O’Neill, L., Seo, H., Song, Q., Cornillon, P., Spall, M. and Minobe, S. (2008), ‘Air–sea interaction over ocean fronts and eddies’, *Dynamics of Atmospheres and Oceans* **45**(3), 274–319.
- Soden, B. J. and Held, I. M. (2006), ‘An Assessment of Climate Feedbacks in Coupled Ocean–Atmosphere Models’, *Journal of Climate* **19**(14), 3354–3360.

- Stone, P. H. (1978), ‘Baroclinic Adjustment’, *Journal of the Atmospheric Sciences* **35**(4), 561–571.
- Thompson, D. W. J. and Li, Y. (2014), ‘Baroclinic and Barotropic Annular Variability in the Northern Hemisphere’, *Journal of the Atmospheric Sciences* **72**(3), 1117–1136.
- Thompson, D. W. J. and Wallace, J. M. (2000), ‘Annular Modes in the Extratropical Circulation. Part I: Month-to-Month Variability’, *Journal of Climate* **13**(5), 1000–1016.
- Thompson, D. W. J., Wallace, J. M. and Hegerl, G. C. (2000), ‘Annular Modes in the Extratropical Circulation. Part II: Trends’, *Journal of Climate* **13**(5), 1018–1036.
- Vallis, G. K., Colyer, G., Geen, R., Gerber, E., Jucker, M., Maher, P., Paterson, A., Pietschnig, M., Penn, J. and Thomson, S. I. (2018), ‘Isca, v1.0: A framework for the global modelling of the atmospheres of Earth and other planets at varying levels of complexity’, *Geoscientific Model Development; Katlenburg-Lindau* **11**(3), 843–859.
- Zurita-Gotor, P. (2008), ‘The Sensitivity of the Isentropic Slope in a Primitive Equation Dry Model’, *Journal of the Atmospheric Sciences* **65**(1), 43–65.
- Zurita-Gotor, P., Blanco-Fuentes, J. and Gerber, E. P. (2013), ‘The Impact of Baroclinic Eddy Feedback on the Persistence of Jet Variability in the Two-Layer Model’, *Journal of the Atmospheric Sciences* **71**(1), 410–429.

Appendix A

Background

A.1 Lorenz energy budgets

We define the Lorenz energy budget equations as in Oort (1964) [53]. Since the dry core without topography has no stationary waves, we omit the transient terms. The definitions for each term in the Lorenz energy budget are provided below, and Table A.1 describes the notation used with each definition.

The mean-component terms are defined as follows:

$$\begin{aligned}G(P_M) &= c_p \int \overline{\gamma [T]^{**} [Q]^{**}} dm \\P_M &= \frac{1}{2} c_p \int \overline{\gamma [T]^{**2}} dm \\C(P_M, K_M) &= - \int \overline{[\omega]^{**} [\alpha]^{**}} dm \\K_M &= \frac{1}{2} \int \overline{([u]^2 + [v]^2)} dm \\D(K_M) &= \int \overline{([u] [F_x] + [v] [F_y])} dm\end{aligned}$$

The eddy-component terms are defined as follows:

$$\begin{aligned}G(P_E) &= c_p \int \overline{\gamma [T^* Q^*]} dm \\P_E &= \frac{1}{2} c_p \int \overline{\gamma [T^{*2}]} dm \\C(P_E, K_E) &= - \int \overline{[\omega^* \alpha^*]} dm \\K_E &= \frac{1}{2} \int \overline{([u^{*2}] + [v^{*2}])} dm \\D(K_E) &= \int \overline{([u^* F_x^*] + [v^* F_y^*])} dm\end{aligned}$$

Table A.1: Notation for the Lorenz energy cycle definitions.

Symbol	Description
P, K	Potential energy, kinetic energy
G, C, D	Generation, conversion, and dissipation operators
M, E	Subscripts denoting the mean, eddy energy components
λ, ϕ	Longitude, latitude
p	Pressure
u, v	Zonal, meridional components of horizontal wind
α	Specific volume
ω	Vertical velocity, $\omega \equiv dp/dt$
T, θ	Temperature, potential temperature, $\theta \equiv T(p_0/p)^\kappa$
F_x, F_y	Frictional acceleration in the zonal, meridional direction
Q	Diabatic heating rate, in units K s^{-1}
a	Radius of spherical Earth, approximately $6.371 \times 10^6 \text{m}$
g	Standard gravitational acceleration, approximately 9.80665m s^{-2}
p_0	Reference pressure, 1000hPa
R_d	Ideal gas constant for dry air, approximately $287 \text{J kg}^{-1} \text{K}^{-1}$
c_p	Specific heat at constant pressure, approximately $1004 \text{J kg}^{-1} \text{K}^{-1}$
κ	Poisson's constant, $\kappa \equiv R_d/c_p \approx 2/7$
Ω	Earth's rotation rate, approximately $7.292 \times 10^{-5} \text{rad s}^{-1}$
f	Coriolis parameter, $f \equiv 2\Omega \sin \phi$
γ	The stability factor, $\gamma(p) \equiv -(p_0/p)^\kappa (R_d/c_p p) (\partial [[\theta]] / \partial p)^{-1}$
\bar{X}	Temporal average of X , equal to $\frac{1}{t_2-t_1} \int_{t_1}^{t_2} X dt$
X'	Deviation from temporal average of X , equal to $X - \bar{X}$
$[X]$	Zonal average of X , equal to $\frac{1}{2\pi} \int_0^{2\pi} X d\lambda$
X^*	Deviation from zonal average of X , equal to $X - [X]$
$[[X]]$	Global average of X , equal to $\frac{1}{2} \int_{-\pi/2}^{\pi/2} [X] \cos(\phi) d\phi$
X^{**}	Deviation from global average of X , equal to $X - [[X]]$
dm	Mass element, equal to $a^2 \cos \phi d\lambda d\phi dp/g$

The eddy-mean conversion terms are defined as follows:

$$\begin{aligned}
C(P_M, P_E) &= -c_p \int \overline{\gamma [v^* T^*]} \frac{\partial [T]}{a \partial \phi} dm \\
&\quad - c_p \int \overline{\gamma \left(\frac{p}{p_0}\right)^\kappa [\omega^* T^*]} \frac{\partial [\theta]^{**}}{\partial p} dm \\
C(K_E, K_M) &= \int \overline{[u^* v^*]} \cos \phi \frac{\partial}{a \partial \phi} \left(\frac{[u]}{\cos \phi} \right) dm \\
&\quad + \int \overline{[u^* \omega^*]} \frac{\partial [u]}{\partial p} dm + \int \overline{[v^* \omega^*]} \frac{\partial [v]}{\partial p} dm \\
&\quad + \int \overline{[v^{*2}]} \frac{\partial [v]}{a \partial \phi} dm - \int \overline{[v] [u^{*2}]} \frac{\tan \phi}{a} dm
\end{aligned}$$

A.2 Spectral decompositions

The data used for the spectral analyses was obtained by taking cyclic Fourier transforms of data on each latitude band, then taking temporal Fourier transforms on 100-day blocks of the resulting Fourier coefficients and averaging 50 of these blocks with a Hanning window. Negative frequencies were taken to indicate *westward* propagation, and positive frequencies were taken to indicate *eastward* propagation.

For the results in section 4.2, we calculated the space-time *spectral power* of the zonal wind anomalies, meridional wind anomalies, and temperature anomalies. We also calculated the space-time *co-spectral power* for “flux” terms: zonal and meridional wind anomalies (corresponding to the eddy-momentum flux), and zonal wind and temperature anomalies (corresponding to the eddy-heat flux). In both cases, negative (positive) co-spectral power indicates net equatorward (poleward) transport of momentum or heat. Spectral decompositions of the Eliassen-Palm flux divergence were found by simply multiplying the co-spectra by the appropriate constants and differentiating them in latitude and pressure (the latitude and pressure dimensions are unaffected by the space-time transform).

The phase speed spectra were obtained by interpolating from *frequency-zonal wavenumber* space to *phase speed-zonal wavenumber* space, as in Randel and Held (1991) [55]. Recall

the phase speed is defined $c_{\text{ph}} \equiv \omega/k$, where ω is the frequency in units s^{-1} and k the zonal wavenumber in units m^{-1} .

A.3 Annular modes

For the climate variability analyses, we considered the following two “annular modes”:

- The **SAM** or barotropic/“southern” annular mode. The SAM is the first empirical orthogonal function (EOF) of the mean-flow kinetic energy field (or, where specified, the zonal-mean zonal wind), and is associated with changes to the *position* of the eddy-driven jet. It is “forced” by variations in *eddy-momentum flux convergence*.

There is of course no statistical difference between northern and southern hemisphere dynamics in the dry core – the “southern” in the SAM simply denotes its symmetry relative to the Arctic oscillation in the real world, owing to the absence of stationary waves due to zonal asymmetries in topography and land coverage.

- The **BAM** or baroclinic annular mode. The BAM is the first EOF of the eddy kinetic energy field (or, where specified, the eddy heat flux), and is associated with changes to the *intensity* of the (mostly baroclinic) eddies. It is “forced” by variations in *isentropic slope*.

The EOF analyses were performed using only northern hemisphere data within the bounds 20°-70° latitude, 250-1000hPa. For details on the annular modes, see Thompson and Li (2014) [68].

The annular mode forcing patterns were found by projecting the PC time series associated with each annular mode onto the corresponding forcing parameter at some characteristic lag (eddy-momentum flux convergence for the SAM, isentropic slope for the BAM). We empirically determined this “characteristic lag” as the time delay for which the projected “forcing pattern” explains the most variance in the corresponding forcing field. For both the BAM and SAM, we considered a range of lags from 0 to 10 days. We found the 1-day

leading pattern of eddy-momentum flux convergence and 5-day leading pattern of isentropic slope explained the largest amount of variance in their respective fields. These patterns were used for the analyses in section 4.4.

The “variance explained” by a stationary pattern was found by comparing the variance in the mass-weighted dot product of the pattern with the full field to the variance in the mass-weighted dot product of the full field with itself. We define the “mass-weighted dot product” as a spatial dot product, weighted by pressure level width and the cosine of the grid box latitude, taken at a single timestep.